Molecular Clock Dating of Deep-Time Evolution Using Complex Mixture Models

Sishuo Wang[1,*], Andrew Meade[2]

1. Department of Microbiology, Faculty of Medicine, The Chinese University of Hong Kong, Hong Kong SAR, China
2. School of Biological Sciences, University of Reading, Reading, UK

* Corresponding author: sishuowang@hotmail.ca

Abstract

Molecular clocks are a fundamental technique in evolutionary biology for establishing the timing and tempo of organismal divergence. However, currently available molecular clock methods, which often rely on simple homogeneous substitution models, can produce inaccurate time estimates, particularly for deep-time or rapidly evolving lineages where substitution heterogeneity and saturation are common. Hereby, we introduce phyloHessian (https://github.com/evolbeginner/phyloHessianWrapper), a Julia-based software to enable the use of complex mixture substitution models in molecular dating. phyloHessian employs different algorithms to improve the numerical accuracy in calculating the phylogenetic Hessian matrix, which is further integrated into PAML-MCMCtree's approximate likelihood framework to conduct dating analyses. Simulations mimicking phylogenies at different timescales demonstrate that complex mixture substitution models significantly enhance the accuracy of divergence time and substitution rate estimates in deep-time phylogenies. This pattern remains consistent across a wide range of uncertainties associated with molecular clock analysis. Additionally, mixture models display greater robustness to model and calibration specifications compared to their homogeneous counterparts. Empirical analysis of Microsporidia and Rickettsiales with different

substitution models shows that mixture models, compared to homogeneous models, yield accelerated substitution rates and in some cases significantly different divergence times, leading to a revised understanding of their host association origins. Our findings underscore the importance of incorporating complex mixture substitution models for constructing reliable evolutionary timelines and elucidating the evolutionary history of deep-time or fast-evolving lineages.

Keywords

molecular clock, PAML, MCMCtree, complex mixture model, deep-time evolution, approximate likelihood, symbiont, pathogen evolution

Introduction

Historically, our understanding of evolutionary time scales relied on limited fossil records, until a significant change occurred in the 1960s when molecular clock theory was proposed (Zuckerkandl and Pauling 1965), making it possible to infer evolutionary time and rate using genetic data. While the original concept of the molecular clock assumed that the rate of gene sequence changes is constant among lineages, further evidence shows that even the same gene can exhibit variations in rate among different species, leading to the development of relaxed molecular clock models which allow for lineage-specific evolutionary rate and a series of derivative models (Thorne et al. 1998; Drummond et al. 2006; Yang and Rannala 2006). Over years, molecular clock theory has evolved, continuously increasing in complexity and accuracy, providing a powerful tool for studying biological evolution. Particularly, with the development of Bayesian phylogenetic methods and the rapid growth of genetic sequence data, Bayesian models based on Markov chain Monte Carlo (MCMC) methods have become the most widely used molecular clock dating method, which allows for a comprehensive examination of various uncertainties in analysis, including factors such as calibrations and across-lineage rate differences (Ho and Duchêne 2014; dos Reis et al. 2016).

While molecular clock approaches offer a powerful framework for inferring evolutionary timescales, the reliability of such inferences heavily depends on accurately modeling the evolution of the molecular data, such as protein sequences, alongside the incorporation of calibration information (Guindon 2020). Protein evolution is typically modelled as site-homogeneous process using empirically derived substitution matrices of amino acid exchangeabilities (e.g., LG or WAG) and fixed equilibrium frequencies, with variation in evolutionary rates modeled with a gamma distribution (Yang 1993). However, while

computationally efficient, such models oversimplify real-world biological processes by failing to capture the heterogeneity in amino acid preferences driven by diverse structural and functional constraints across sites. To address these issues, site-heterogeneous substitution models have been proposed since (Lartillot and Philippe 2004; Pagel and Meade 2004). These models account for among-site substitution heterogeneity by incorporating predefined substitution matrices for different secondary structures and solvent accessibility (Le et al. 2008; Le and Gascuel 2010), across-site rate variation (Le et al. 2012), or mixtures of amino acid frequency profiles (Quang et al. 2008; Wang et al. 2008). Of particular interest is the last category, which captures different amino acid preferences across sites, as represented by the CAT model (Lartillot and Philippe 2004) and its simplified counterparts for maximum-likelihood phylogenetics called Cxx (where xx indicates 10 to 60 profile categories) (Quang et al. 2008). By better approximating the true biological complexity of amino acid substitution, profile mixture models mitigate artifacts like long branch attraction, thereby enhancing the ability to distinguish phylogenetic signal from homoplasy and displaying higher sensitivity to substitution saturation (Wang et al. 2018; Wang et al. 2019; Schrempf et al. 2020; Baños, Susko, et al. 2024). These features make profile mixture models especially well-suited for studying microbial evolution, where deep divergences and rapidly evolving sites are prevalent. Indeed, empirical analyses of deep-time phylogenomic data show that profile mixture models often exhibit superior model fit compared to homogeneous alternatives (Williams et al. 2020; Bujaki and Rodrigue 2022).

A particular outcome of using site-homogeneous models like LG+G is that branch lengths are usually underestimated in case of extensive sequence divergence (Venditti et al. 2008; Moody et al. 2022). This happens because proteins may not use all 20 amino acids at each position and homogenous models incorrectly interpret this restricted use of amino acids as evidence of less

evolutionary change than what truly occurred over long time (Lartillot et al. 2007; Wang et al. 2008). To see this, consider a site restricted to Asp and Glu. A mixture model would identify a preference for negatively charged amino acids and infer unobserved substitutions (e.g., Asp → Glu → Asp) even if two sequences show the same amino acid, leading to longer branch lengths. Obviously, this pattern becomes more readily observed with an increasing evolutionary scale. Studies have shown that the deepest branches of the tree of life, spanning approximately 4.0 billion years (Gyr), can display branch lengths up to twice as long under profile mixture models compared to the LG+G model (Moody et al. 2022; Wang and Luo 2025). Given that in molecular clock analysis branch length, the expected substitutions per site, is the product of time and (average) substitution rate of that branch (dos Reis et al. 2016; Guindon 2020), an important question emerges: do profile mixture models, which often excel in deep-time phylogenetic inference, lead to more accurate divergence time and substitution rate estimates?

To our knowledge, none of the available molecular clock programs have directly implemented complex substitution models including those profile mixture models, with PhyloBayes' CAT model being the exception—yet its high computational demands limit its use in large-scale molecular clock analyses. We recently developed bs_inBV (Wang and Luo 2025), enabling the use of diverse substitution models in the popular MCMCtree molecular dating software by applying a bootstrap approximation of the Hessian matrix, which captures likelihood surface curvature and is required by MCMCtree's fast approximate likelihood dating procedure (Thorne et al. 1998; dos Reis and Yang 2011). However, the bootstrapping process is computationally intensive, and its approximation sometimes inadequately represents the true Hessian. Additionally, and perhaps more importantly, the relative performance of different substitution models in molecular clock dating remains unexamined through systematic

simulation studies, leaving a critical gap in our understanding of how choice in substitution model affects divergence time estimation, particularly in deep-time or fast-evolving phylogenies.

Hereby, we introduce phyloHessian, a Julia-based software that uses numerical methods to calculate accurate Hessian matrices for diverse complex substitution models and integrates them directly into MCMCtree's approximate likelihood framework for rapid molecular clock dating. We perform extensive analyses on simulation data to comprehensively compare the performance of different substitution models in divergence time and substitution rate estimation under a wide range of conditions that mimic phylogenies from relatively recent to very ancient divergences. We further analyze empirical data to assess how different substitution models affect our understanding of ancient symbiont evolution and the origins of their host associations.

Results

phyloHessian: enabling molecular clock dating in MCMCtree with complex substitution models

To address the challenges in molecular clock analysis under various substitution models, we developed a Julia-based software phyloHessian. phyloHessian first calls IQ-Tree (Wong et al. 2025) or PhyML (Guindon et al. 2010), two widely used phylogenetic reconstruction software that implement a range of mixture models, to calculate the maximum-likelihood estimates (MLE) of branch length $\hat{\theta} = \left(\hat{\theta}_1, \dots, \hat{\theta}_n\right)^{\mathrm{T}}$ under user-specified substitution model. Let $\theta = (\theta_1, \dots, \theta_n)$ be the branch lengths and $\Delta\theta = \theta - \hat{\theta}$. Next, it applies finite difference numerical methods to calculate the gradient $g = \left(\frac{\partial \ell(\hat{\theta})}{\partial \theta_1}, \dots, \frac{\partial \ell(\hat{\theta})}{\partial \theta_n}\right)^{\mathrm{T}}$ and Hessian matrix $H\left(\hat{\theta}\right) = \left(\frac{\partial^2 \ell(\hat{\theta})}{\partial \theta_i \partial \theta_j}\right)$, i.e., the first- and second-order derivatives of the log-likelihood of the phylogenetic data

evaluated at the MLEs. . Last, the resulting Hessian matrix is integrated into MCMCtree to be used with its approximate likelihood method (Thorne et al. 1998; dos Reis and Yang 2011) for divergence time and rate estimation. MCMCTree's approximate likelihood method approximates the log-likelihood surface for branch lengths using a Taylor expansion to the second order

$$\ell(\theta) \approx \ell(\hat{\theta}) + \mathrm{g}^{\mathrm{T}}\Delta\theta + \frac{1}{2}\Delta\theta^{\mathrm{T}} H(\hat{\theta})\Delta\theta.$$

To demonstrate the reliability of phyloHessian, we compared its results with those obtained from well-established phylogenetics software packages. First, we found that phyloHessian and IQ-Tree produced identical log-likelihoods under all tested complex substitution models available in IQ-Tree (Data S1). Further, we validated phyloHessian's Hessian calculation by confirming that the Hessian matrix obtained by phyloHessian and CODEML under site-homogeneous models (such as LG+G) were nearly identical (Data S2).

Profile mixture substitution models enhance time and rate estimation in deep-time and fast-evolving phylogenies: evidence from simulations

To evaluate the impact of mixture substitution models (Materials and Methods: Mixture substitution model) on divergence time and substitution rate estimates, and to compare their performance to profile homogeneous models like LG+G, we conducted extensive simulations. To simulate a range of evolutionary scenarios spanning relatively recent to very deep-time divergences, we followed our prior study (Wang and Luo 2025) to generate 30 replicates of 20-tip birth-death trees with protein sequences that were 300 amino acids (aa) in length simulated under the substitution model LG+C60+G4{1.0} for both autocorrelated-rates (AR) and independent-rates (IR) molecular clock rate model. For simplicity, we use "+G" to represent "+G4{1.0}" hereafter [IQ-Tree's default; four-category discrete Gamma distribution for the

relative rate, shape parameter α = 1.0, i.e., Gamma(1,1)]; see also Materials and Methods: Simulation procedure. We mainly focused on five calibration strategies. These five calibration strategies consisted of a single calibration at the root with both upper and lower bounds (*root*), fully calibrated root plus one fully-bounded internal node (*calib-1_0.2*), fully calibrated root plus one minimum-bounded internal node (*calib-1_0.2--only_min*), fully calibrated root plus two fully-bounded internal nodes (*calib-2_0.2*), and fully calibrated root plus two minimum-bounded internal nodes (*calib-2_0.2--only_min*).

Under the focal simulation scheme (see Materials and Methods: Simulation procedure), the profile mixture model LG+C60+G performed comparably to the traditional LG+G model for divergence time estimation when simulated root ages were set to either 1.0 or 2.0 billion years ago (Ga). However, for root ages ≥3.0 Ga, LG+C60+G obtained significantly more accurate time estimates than LG+G, with the performance gap becoming increasingly pronounced at 4.0 Ga (Fig. 1A). For example, under the *root* calibration strategy, LG+C60+G demonstrated superior time estimation accuracy (mean relative difference ± SD: 0.157 ± 0.061 for AR clock model, 0.139 ± 0.046 for IR clock model) compared to LG+G (AR: 0.193 ± 0.062; IR: 0.197 ± 0.061). Mean relative difference is defined as mean $\left(\frac{|b_i^m - b_i^{true}|}{\max(b_i^m, b_i^{true})}\right)$, where b_i^m and b_i^{true} respectively denote the inferred posterior mean age and the true value for node i. The largest discrepancies in divergence time estimation occurred under the calibration scheme "*two_min*", where LG+C60+G showed lower error than LG+G (mean relative difference: AR 0.160 vs. 0.232; IR 0.147 vs. 0.259; Fig. 1A). In contrast to divergence time estimates, LG+C60+G provided much more accurate branch-specific substitution rate estimates than LG+G across all tested root ages (Fig. 1B). The error reduction obtained by LG+C60+G compared with LG+G, calculated as $\frac{\text{reldiff}_{\text{LG+G}} - \text{reldiff}_{\text{LG+C60+G}}}{\text{reldiff}_{\text{LG+G}}}$, averaged across all calibration strategies, ranged from 26% to 53%

172 under AR, and 23% to 55% under IR for root ages of 1.0 to 4.0 Ga (Table 1). The pattern held
173 true with alternative metrics for comparison with the simulation values (Figs. S1-S3).
174 Next, we explored the patterns for more complex mixture models. We combined structurally
175 constrained substitution models EX2 (exposed/buried sites) and EX3 (highly
176 exposed/intermediate/buried sites) (Le et al. 2008) with the predefined equilibrium frequency
177 C20 to account for site-specific variation in amino acid profiles by 20 categories of equilibrium
178 frequencies. This resulted in 40 and 60 different rate matrices for EX2 and EX3 respectively.
179 When simulation was done under profile-exchangeability mixture models EX2+C20+G and
180 EX3+C20+G, the above patterns became more pronounced (Fig. S4). In contrast to profile
181 mixture models, when alignments were simulated under exchangeability mixture models
182 (EX2+G, EX3+G, and LG4M), LG+G and the true simulation model performed similarly in
183 estimating divergence times and evolutionary rates (Fig. S5).
184 Large sequence divergence may arise from not only long divergence time, but also rapid
185 evolution. To test whether different time estimates are affected by varying evolutionary rates
186 (Fig. S6), we simulated alignments on phylogenies with a fixed root age of 1.0 Ga but different
187 mean absolute substitution rates along the phylogeny (0.25-1.0 substitutions/site/Gyr). This
188 represents evolutionary rates from relatively low, as in most microbes, to very fast, as observed
189 in some pathogens. We would anticipate comparable sequence divergence whether we fixed the
190 root age at 1.0 Ga and increased the average substitution rate (from 0.25 to 1.0
191 substitutions/site/Gyr; Fig. S6), or fixed the substitution rate at 0.25 substitutions/site/Gyr and
192 increased the root age to 4.0 Ga (Fig. 1). Averaged across all calibration strategies, LG+C60+G
193 displayed error reductions in substitution rate estimate of 65% (AR) and 61% (IR) at a mean
194 substitution rate of 1.0 substitutions/site/Gyr.

195

196 **Performance of profile mixture models in molecular clock dating under varied simulation**
197 **conditions**

198 Next, we evaluated the influence of multiple sources of uncertainties in molecular clock dating
199 on the performance of profile mixture and traditional homogenous models when sequence
200 alignments are simulated under profile mixture models. These involve sequence length, Gamma-
201 distributed across-site rate, birth-death process, variance in lineage-specific rates, and number of
202 sequences (see Note S1 for details).

203 We first investigated how sequence length (ranging from 100 to 2000 aa) affected the
204 accuracy of the estimates using different substitution models (Fig. S7). Although the increase in
205 divergence time estimate accuracy achieved by using LG+C60+G instead of LG+G was minimal
206 for 100-aa alignments, the improvement became increasingly apparent as the alignment length
207 extended to 2000 aa. Across all analyzed calibration strategies, the LG+C60+G model
208 consistently improved the accuracy of time estimation for the AR clock models compared to
209 LG+G. For a simulated root age of 4.0 Ga, this improvement was substantial, resulting in an
210 error reduction (see above) of 30%, 28%, 25%, and 12% for alignment lengths of 2000, 1000,
211 500, and 100 aa, respectively; the benefit was still significant but less pronounced for a younger
212 root age of 3.0 Ga, with corresponding improvements of 22%, 18%, 15%, and 7%. Both
213 LG+C60+G and LG+G models achieved higher estimation accuracy with longer sequences (i.e.,
214 lower values in *y*-axis from 100 to 2000 aa), indicating that longer sequences are more
215 informative for more accurate molecular clock analyses, consistent with the notion that mixture
216 models perform much better on longer alignments for phylogenetic reconstruction (Baños,
217 Susko, et al. 2024).

We further adjusted the gamma correction parameter (α) to modulate the variance of the across-site relative rates. Specifically, we set α to 0.5 and 1.5, which scaled the across-site variance to 2-fold ($0.5/0.5^2$) (scheme *Gamma_0.5* in Fig. 2A) and 2/3-fold ($1.5/1.5^2$) (scheme *Gamma_1.5* in Fig. S9A), respectively, compared to our focal analysis (α=1). These adjustments did not alter the patterns observed in the original analysis. Similarly, when exploring alternative birth-death process parameters, a flat birth-death process (simulation scheme: *bd_flat*) produced results comparable to those from the focal analysis (Fig. 2B). Under complete species sampling (100%), the difference in time estimates between the LG+G and LG+C60+G models became more obvious (scheme *bd_0.4-0.2-1* in Fig. S9B). Moreover, increasing the standard deviation of the among-branch sequence absolute substitution rate to twice and three times its default value reduced the differences in divergence time estimation between using LG+G and LG+C60+G, despite the unchanged overall pattern (schemes *sigma_0.38, sigma_0.55* in Figs. 2C, S9F). In addition, although all simulations above were performed on 20-tip trees for simplicity, the analysis was extended to 40-, 60-, 80-, and 100-tip trees, with similar patterns found (Fig. S10).

Profile mixture models display higher robustness to model misspecification

Further, we applied simulations to test the robustness of profile mixture models to misspecifications in calibrations or substitution models. To explore whether mis-specified calibrations would affect estimation under different substitution models when the sequences were simulated under LG+C60+G, we calibrated the nodes by adjusting their ages. These adjustments consisted of fixed percentage increases (shifting ages toward the past) or decreases (shifting ages toward the present) (Fig. 3). In general, LG+C60+G achieved higher accuracy when calibrations were older than the true divergence times (Fig. 3B). For a root age of 4.0 Ga and across all tested

241 calibration strategies, on average, the relative difference in time estimation compared to true
242 values was: 0.256 (LG+G) versus 0.195 (LG+C60+G) for the AR model, and 0.278 (LG+G)
243 versus 0.185 (LG+C60+G) for the IR model. For root age of 3.0 Ga, these values changed to
244 0.252 (LG) versus 0.202 (LG+C60+G) for AR, and 0.255 (LG) versus 0.192 (LG+C60+G) for
245 IR (Fig. 3B). Subtle differences between using LG+G and LG+C60+G were observed for root
246 age ≤ 2.0 Ga. However, when calibrations were biased towards younger ages, the LG+G and
247 LG+C60+G models generally yielded comparable accuracy for divergence time and substitution
248 rate estimates, irrespective of the root age, with significant differences arising occasionally.
249 The above analyses focused on alignments simulated under complex substitution models,
250 particularly LG+C60+G. To determine how these models perform in molecular clock analysis
251 when sequences evolve under simpler substitution models, we performed additional simulations
252 using these models and the previously described settings (varying the simulated root ages from
253 1.0 to 4.0 Ga (Fig. 3B). These analyses indicate that the profile mixture model LG+C60+G
254 displayed robust time and rate estimation, regardless of the true underlying substitution process.
255 The robustness of LG+C60+G is evident in the following comparisons. When sequences were
256 simulated under the basic LG+G model, LG+C60+G provided estimates of divergence times and
257 absolute substitution rates at least as accurate as those obtained using LG+G. Further, similar
258 results were observed when simulations were conducted with other models with factors not
259 explicitly modeled by LG+C60+G, such as invariant sites (+I) and free rate across-site
260 heterogeneity (+R) (Note S1). These findings suggest that LG+C60+G's robustness was
261 maintained even when the true evolutionary process involves additional complexities in
262 substitution models.
263

Comparison between profile mixture models with PMSF (posterior mean site frequency) and bootstrapped-Hessian approximations in molecular clock dating

The computational intensity of the LG+C60+G model often necessitates the PMSF approximation to accelerate phylogenetic reconstruction, especially for large datasets (Wang et al. 2018). This occurs because PMSF requires the computationally intensive pruning algorithm to run only once per site pattern using an approximated equilibrium frequency, versus *c* times for a mixture model with *c* classes. A distinct approximation, previously employed in molecular clock analyses under complex substitution models, uses a bootstrap-based method to approximate the Hessian matrix and is implemented in the software bs_inBV (Wang and Luo 2025). To assess the impact of these two approximations on molecular clock dating under profile mixture models, we compared divergence time and substitution rate estimates derived with each approach against those obtained with the full Hessian matrix calculated without either approximation. We found that both approximations provided accurate estimates of divergence times, no matter which root age was used in simulation (Fig. 4A). In terms of the time estimates, across all simulated root ages, compared to LG+C60+G estimated rates, the average differences for AR were 3.6 ± 1.0% (PMSF approximation; *LG+C60+G+PMSF*), 7.1 ± 0.6% (bootstrapped-hessian; *LG+C60+G+bs_inBV*), and 7.3 % 0.8% (combined use; *LG+C60+G+PMSF+bs_inBV*); for IR, the differences were 1.8 ± 0.4%, 5.9 ± 0.4%, and 6.5 ± 0.5%, respectively. The deviations in time estimates from these approximations, particularly PMSF, were close enough to the stochastic variation observed across independent MCMC runs of the original profile mixture model (*LG+C60+G_run2* in Fig. 4; baseline in Fig. 4 consists of times and rates from initial MCMC run under LG+C60+G). The estimates of evolutionary rates exhibited slightly greater divergence from the original model with either approximation (Fig. 4B). Compared to rates estimated under

287 the LG+C60+G model without any approximation, the mean relative differences under both AR
288 and IR models were around 8% for either approximation, or their combination.
289
290 **Divergence times and substitution rates under mixture models for the ancient symbionts**
291 **Microsporidia and Rickettsiales: an empirical study**
292 To evaluate mixture models on empirical data, we selected two ancient symbiont lineages with
293 distinct evolutionary significance and accelerated evolutionary rates: Microsporidia, highly
294 reduced, fast-evolving obligate intracellular parasites of animals related to fungi (Capella-
295 Gutiérrez et al. 2012), and Rickettsiales, an alphaproteobacterial lineage that shares a close
296 evolutionary relationship with the ancestors of mitochondria (Martijn et al. 2018; Wang and Luo
297 2021). Their rapid evolution combined with ancient divergence makes them ideal test cases for
298 our analysis. Note that our primary goal was to assess how complex substitution models
299 influence the molecular clock analysis itself, leading us to test different settings rather than
300 selecting a single optimal configuration (e.g., partitions, clock model).
301 For both datasets, we partitioned the alignments into three subsets (see Materials and
302 Methods) according to a Gaussian mixture model-based clustering according to the logarithm of
303 the estimated substitution rates of each gene, and selected the best-fitting substitution models for
304 each partition under both site-homogeneous and mixture substitution models respectively. In all
305 cases, profile mixture models were associated with the lowest AIC values, with
306 LG+Cxx+F+I+R4 (where xx = 40, 50, 60) being the most frequently selected (Data S3-S4).
307 Microsporidia do not have fossil records. Thus, we applied different calibrations to only the root
308 node based on previous estimate of the occurrence time of its LCA (last common ancestor) (Note
309 S2). We found that the time estimates for Microsporidia lineages were largely consistent between

310 the best-fitting profile mixture and homogenous models (Fig. 5). The LCA of Microsporidia was
311 estimated to occur at approximately 0.41 Ga (95% HPD: 0.74-0.45 Ga) and 0.63 Ga (95% HPD:
312 0.73-0.52 Ga) under the AR and IR clock models, respectively (Fig. 5A). In contrast to the
313 similar divergence time estimates between homogeneous and mixture models, the absolute
314 substitution rate was at least 1/3 higher under the mixture model (Fig. 5B). All microsporidian
315 lineages experienced accelerated sequence changes compared to the outgroup lineages. While the
316 highest substitution rate was predicted for the branch leading to the LCA of Microsporidia under
317 the IR clock model, the AR clock model instead predicted the highest rate on the branch leading
318 to *Enterocytozoon*, a major microsporidian pathogen in human and animals. The above pattern
319 was consistent with alternative calibrations and different numbers of partitions (Fig. S11).
320 Rickettsiales also lack direct fossil evidence; however, due to their close phylogenetic
321 relationship with mitochondria, we employed the mitochondrial endosymbiosis dating strategy as
322 used in our prior study (Wang and Luo 2021). This approach allows estimating Rickettsiales'
323 evolutionary timeline by incorporating eukaryotic fossils, based on the evolutionary scenario that
324 mitochondria evolved from a lineage closely related to Alphaproteobacteria (and thus
325 Rickettsiales). Particularly, under the AR clock model, the time estimates of Rickettsiales
326 lineages under the mixture substitution model differed by an average of >20% compared to those
327 from the homogeneous alternatives (Fig. 6A). In general, the ages of most lineages were
328 estimated to be older under the profile mixture model (Fig. 6A). For example, under the AR
329 clock model, the LCA of Rickettsiales was estimated to occur at 2.67 Ga (95% HPD: 2.97-2.35
330 Ga) by the mixture model, whereas the homogeneous substitution model estimated it at 2.26 Ga
331 (95% HPD: 2.57-1.94 Ga). Similarly, eukaryotes were estimated to originate at 2.29 Ga (95%
332 HPD: 2.57-1.98 Ga) under the mixture model, compared to 1.74 Ga (95% HPD: 1.98-1.50 Ga)

333 under the homogeneous model (Fig. 6A). The above pattern holds under alternative calibration
334 settings (Fig. S12). With a single partition (Fig. S12A, S12B), the difference in time estimates
335 between different substitution models was less obvious. In all calibration schemes, the
336 substitution rates under the mixture models were roughly 1.5 to 2 times those estimated under
337 homogeneous models (Fig. 6B).
338 A recent study (Baños, Susko, et al. 2024) suggests that the empirical frequency estimated
339 from the alignment (+F) might mislead phylogenetic reconstruction for profile mixture models.
340 As an additional analysis, we re-performed molecular clock dating with the best-fitting mixture
341 model without the empirical frequency option. Similar patterns were found (Figs. S13-S14).
342

343 **Discussion**

344 **Approximate likelihood dating with complex models**

345 The present study introduces phyloHessian, enabling Hessian calculation under diverse mixture
346 and non-mixture amino acid substitution models for molecular clock dating using MCMCtree's
347 approximate likelihood method (Thorne et al. 1998; dos Reis and Yang 2011). A key question is
348 whether MCMCtree's approximate likelihood method performs equally well as exact likelihood
349 under mixture substitution models in terms of divergence time estimation. While previous
350 research suggests that this holds true for homogeneous models (dos Reis and Yang 2011), a full
351 comparison is impossible due to the lack of software directly implementing complex substitution
352 models. Therefore, we compared the phylogenetic likelihoods of bootstrap trees calculated by the
353 approximate and exact likelihood methods under LG+C60+G using phyloHessian. The
354 approximate likelihood values obtained from phyloHessian (using finite differences) generally
355 showed good agreement with those derived from both the exact method and bs_inBV, despite

some minor discrepancies. (Fig. S15). Further, phyloHessian sometimes outperformed bs_inBV, with bs_inBV showing markedly lower lnL in occasional cases. (Fig. S15). Discrepancies in time and rate estimates between the Hessian-based method (phyloHessian) and the bootstrap approximation (bs_inBV) stem from three factors (Fig. 4): the inherent limitation of bs_inBV due to the finite number of bootstrap replicates; the statistical assumption in bs_inBV that the gradient is zero when approximating the Hessian via the covariance matrix, an assumption that is invalid when the MLEs of branch lengths are near zero (dos Reis and Yang 2011); and the difference in parameter handling, as MCMCtree fixes substitution model parameters (such as the parameter α for the gamma distribution for relative rates) at their MLEs while bs_inBV re-estimates all parameters in each bootstrap, resulting in phyloHessian using only the branch length Hessian versus bs_inBV approximating the full parameter Hessian. A more thorough examination in time estimates, instead of the phylogenetic likelihood, is necessary to fully address the question in future.

It was when we were finishing writing this manuscript that another computational software IQ2MC (Demotte et al. 2025) implemented in the newest version of IQ-Tree (v3.0.1) (Wong et al. 2025), became available on a preprint server. IQ2MC leverages the highly efficient computation of IQ-Tree's phylogenetic library to estimate the Hessian matrix under not only amino acid, but nucleic acid and partitioned models, unlike PhyloHessian which is restricted to amino acid models. IQ2MC was roughly 3X and 10X times faster than CODEML and phyloHessian respectively (Data S5). However, our software, phyloHessian, offers more flexible settings in molecular dating by alternative Hessian calculation algorithms and interactions with other software like PhyML and bs_inBV. Its code for phylogenetic likelihood calculation under

complex substitution models would be a valuable resource for phylogenetic software development within the Julia ecosystem.

Other methods, such as McmcDate (Mahendrarajah et al. 2023), also accelerate molecular dating analyses by approximating the phylogenetic likelihood. It is in concept similar to bs_inBV (Wang and Luo 2025), but operates in a Bayesian framework. A key advantage of bs_inBV and McmcDate over phyloHessian and IQ2MC is their ability to accommodate substitution models not yet available in specific phylogenetics software, such as FunDi (Gaston et al. 2011) or CAT-PMSF (Szánthó et al. 2023). However, these approximations via bootstrap or MCMC sampling may sacrifice computational speed and accuracy to some extent (Fig. 4), as discussed above.

Deep-time molecular clock dating: the influence of complex mixture models

Our extensive simulations demonstrate that the advantage of using the complex mixture substitution model for divergence time estimation becomes increasingly significant as evolutionary timescales deepen (Figs. 1-4). Particularly, when the root age was earlier than 2.0 Ga, the difference became obvious. This highlights the importance of substitution models that better fit the data for dating deep-time phylogenies. On the other side, the substitution rate was almost always estimated higher and more accurate under mixture models than under homogeneous models. The underlying logic is straightforward. Mixture models typically estimate longer branch lengths than homogeneous models (Venditti et al. 2008; Moody et al. 2022; Wang and Luo 2025). Because branch length equals substitution rate multiplied by time (dos Reis et al. 2016; Guindon 2020), the underestimated branch lengths under simpler substitution models must be attributable to changes in either the rate, the time, or both. Given that molecular clock analyses typically constrain the time estimates through fossil-based

401 calibrations, the increased branch lengths under mixture models primarily result in higher rate
402 estimates, with a smaller impact on the time estimates themselves.
403 The case in empirical data analysis is more complex. Unlike simulations with known
404 parameters, empirical data could arise from processes so complex that even the best-fitting
405 models are inadequate. This notion is supported by the frequent selection of the most highly
406 parameterized models as the best fit, implying that the complexity of the real process the
407 sequence is generated far exceeds the capabilities of our current models. Consequently, they
408 could make little difference in the time estimates compared to homogeneous models, because
409 both might be an oversimplification of the true model. In such cases, it would be worth applying
410 models like UDM (Schrempf et al. 2020) with more profile mixtures than C60, or the GTRpmix
411 exchangeability matrix and its derived models (Baños, Wong, et al. 2024). While these models
412 have been integrated into phyloHessian, a comprehensive evaluation of their applications in
413 molecular dating analysis on empirical data remains a task for future research.
414 While the "mean relative difference" metric used to compare between models takes the
415 absolute value, it is possible to tell a presumable bias in the time estimates from Figs. S2-S3: the
416 posterior ages estimated by the homogeneous model seemed to overestimate the divergence
417 times in scenarios mimicking deep-dating evolution in simulation. As such, it would be very
418 important to have appropriate maximum time bounds on internal nodes (Wang and Luo 2021;
419 Moody et al. 2022). If indeed in current molecular clock models there is a systematic bias in
420 overestimating the divergence times, it might also explain the observation that mixture models
421 displayed greater improvements in time estimation in the absence of maximum time bounds
422 (*single_min*, *two_min*) compared to the case where internal nodes are fully calibrated
423 (*single_interval*, *two_intervals*; Fig. 1A). In contrast to simulations, the Rickettsiales data reveals

424 a contrasting pattern where mixture models led to older age estimates (Fig. 6). We suspect that
425 one important factor lies in the calibration settings. In simulations, we have complete control
426 over the calibration settings. Real-world data introduces complexities absent in simulation
427 because the available calibrations are not uniform in their quality. While some might accurately
428 reflect the true age of the node, others could be overly young, overly old, or simply
429 uninformative. This complex interplay between substitution models and the quality and number
430 of time calibrations, along with other variables such as the clock model and sequence length,
431 likely makes the impact of mixture substitution models on posterior age estimates case
432 dependent.

433 In summary, while the present study indicates significant impacts of complex profile
434 mixture substitution models on divergence time inferences for deep-time or fast-evolving
435 lineages, the importance of these models on time estimates cannot be overstated; their effect
436 likely requires consideration on a dataset-specific basis. Therefore, we recommend rigorous
437 molecular clock analyses employing different substitution models to assess their impact on
438 divergence time and substitution rate estimates in future research. Note also that while our
439 simulations used an LG+C60+G model, the LG exchangeabilities themselves were not estimated
440 in the presence of profile mixtures (Le and Gascuel 2008). Ideally, for practical applications, it
441 would be more appropriate to use models that directly estimate exchangeabilities under a
442 corresponding profile mixture model for such cases (Baños, Wong, et al. 2024).
443

444 **Implications for the evolution of ancient symbionts**

445 For empirical datasets of Microsporidia and Rickettsiales, profile mixture models, which display
446 much higher model fit to data than their homogeneous counterparts, produced significantly

447 higher substitution rates than estimated by homogeneous models (Figs. 5B, 6B). The difference
448 suggests that bacterial pathogens/symbionts could experience relatively high evolutionary rates
449 up to 1.0 or 2.0 Gyr. This hints that factors like elevated mutation rates, selection, or persistently
450 reduced effective population sizes, which are often responsible for rapid sequence divergence,
451 can have more profound and long-lasting effects on the evolutionary trajectory of symbiotic
452 microorganisms than previously thought. Studying the substitution rates will also improve our
453 understanding of microbial lifestyle evolution.

454 One of the merits of the mitochondria symbiosis-based dating method for Rickettsiales
455 evolution is that it co-estimates the divergence times for both Rickettsiales and their eukaryotic
456 hosts with a unified dataset (Wang and Luo 2021). Notably, under profile mixture models, the
457 origin time of Rickettsiales was estimated at 2.5-2.0 Ga, roughly 0.5 Gyr earlier than that of the
458 last eukaryotic common ancestor (LECA) using homogeneous models estimated in both the
459 current (Fig. 6) and previous studies (Parfrey et al. 2011; Betts et al. 2018; Wang and Luo 2021;
460 Moody et al. 2024). Hence, if the revised time estimate is accurate, it implies that the
461 Rickettsiales' LCA existed before LECA emerged. This interpretation is consistent with recent
462 comparative genomics findings suggesting that early Rickettsiales initially adopted a free-living
463 or non-obligate symbiotic lifestyle (Castelli et al. 2024), with subsequent evolutionary events
464 leading to independent colonizations of eukaryotic hosts—first protists, then animals (Castelli et
465 al. 2016; Wang and Luo 2021). Alternatively, it is possible that early Rickettsiales were
466 associated with unknown host organisms belonging to eukaryotic stem groups (i.e., extinct or
467 unknown lineages that diverged before LECA but after the split with the closest living relatives
468 of eukaryotes). This hypothesis points to previously unrecognized interactions between stem-

group eukaryotes and prokaryotes, and hints at complex prokaryotic engagement as a foundational trait of eukaryotic ancestors, offering insights into the origin of eukaryotes.

Materials and Methods

Mixture substitution model

In a mixture model, each category consists of a rate matrix M, an equilibrium frequency vector F, and a relative substitution rate R. Additionally, the computation of the likelihood necessitates the inclusion of branch lengths θ, and the tree topology τ. Let the full parameter vector be denoted by $\mathbf{\Theta} = (R, F, V, \theta, \tau)$. Denote by $\mathcal{R}$, $\mathcal{F}$, and $\mathcal{V}$ the number of categories of exchangeability matrices, equilibrium frequencies, and relative substitution rates, respectively. Denote by $\mathcal{S}$ the number of alignment sites. Hence, the full likelihood of the phylogeny is given as

$$P(D|\mathbf{\Theta}) = \prod_{s=1}^{\mathcal{S}} \sum_{r=1}^{\mathcal{R}} \sum_{f=1}^{\mathcal{F}} \sum_{v=1}^{\mathcal{V}} P\left(D_s \middle| R_r, F_f, V_v, \theta, \tau\right) P\left(R_r, F_f, V_v\right), \tag{1}$$

where $P\left(R_r, F_f, V_v\right)$ indicate the mixture weights (Guindon 2019). Generally, one might define unnormalized weights $w_{rfv} = P(R_r)P\left(F_f\right)P(V_v)$ assuming independence. Model constraints are imposed by setting $w_{rfv} = 0$ for disallowed combinations $(\mathrm{r}, \mathrm{f}, \mathrm{v})$, such that the final weights are normalized as $P\left(R_r, F_f, V_v\right) = \frac{w_{rfv}}{\sum_{r,f,v} w_{rfv}}$. Specifically, in the common case of independence across components, combinations are allowed, resulting in $P\left(R_r, F_f, V_v\right) = P(R_r)P\left(F_f\right)P(V_v)$, while for models that link equilibrium frequencies and relative rates (e.g., LG4M/LG4X), the constraint is imposed by setting $w_{rfv} = 0$ if $f \neq v$.

Numerical calculation of the Hessian matrix

Two primary numerical methods are commonly employed for computing the Hessian matrix. Let $\hat{\theta} = (\hat{\theta}_1, \dots, \hat{\theta}_n)$ indicate the vector of the MLES of branch lengths, and $\ell(\hat{\theta})$ be the log-likelihood of the phylogeny. The outer product of scores (OPS) method (Seo et al. 2004; dos Reis and Yang 2011) estimates the Hessian matrix indirectly using the first derivatives (scores) of the log-likelihood to sum the contributions of the log-likelihood at each site:

$$H(\hat{\theta}) \approx -\sum_{s=1}^{S} \left(\frac{\partial}{\partial \theta} \ell_s(\hat{\theta}) \frac{\partial}{\partial \theta^T} \ell_s(\hat{\theta}) \right). \tag{2}$$

Each component of the score vector $\frac{\partial}{\partial \theta} \ell_s(\hat{\theta})$ is numerically calculated by the central finite difference method as

$$\frac{\partial \ell_s}{\partial \theta_i} \approx \frac{\ell_s(\hat{\theta} + he_i) - \ell_s(\hat{\theta} - he_i)}{2h} + \mathcal{O}(h^2),$$

where e_i is the i-th standard basis vector, and h is a small step size, typically the cube or square root of machine precision.

The second way is by a direct second-order derivative method. It calculates $H(\hat{\theta})$ via finite differences of the log-likelihood function by

$$H(\hat{\theta}) = \sum_{s=1}^{S} \frac{\partial^2}{\partial \theta \partial \theta^T} \ell_s(\hat{\theta}), \tag{3}$$

where diagonal elements and off-diagonal elements are respectively calculated by the central finite difference method as

$$H_{ii}(\hat{\theta}) \approx \frac{\ell(\hat{\theta} + he_i) - 2\ell(\hat{\theta}) + \ell(\hat{\theta} - he_i)}{h^2},$$

$$H_{ij}(\hat{\theta}) \approx \frac{\ell(\hat{\theta} + he_i + he_j) - \ell(\hat{\theta} + he_i - he_j) - \ell(\hat{\theta} - he_i + he_j) + \ell(\hat{\theta} - he_i - he_j)}{4h^2}.$$

Under regularity conditions, $H(\hat{\theta})/\mathcal{S}$ converges to the expected Fisher information for a single site $I(\theta) = -\mathrm{E}\left[\frac{\partial^2}{\partial\theta\,\partial\theta^T}\ell_s(\theta)\right]$ regardless of whether it is calculated using Eq. (2) or (3) (Pawitan 2001):

$$\frac{\mathbf{1}}{\mathcal{S}}\sum_{s=1}^{\mathcal{S}}\frac{\partial^2}{\partial\theta\partial\theta^T}\ell_s(\hat{\theta}) \simeq -\frac{\mathbf{1}}{\mathcal{S}}\sum_{s=1}^{\mathcal{S}}\left(\frac{\partial}{\partial\theta}\ell_s(\hat{\theta})\frac{\partial}{\partial\theta^T}\ell_s(\hat{\theta})\right). \tag{4}$$

In both methods described as above, the error term is of order $\mathcal{O}(h^2)$. To further improve the numerical accuracy of the second-order derivative method, particularly when dealing with very short branches, we derive the central finite difference calculation of the Hessian at $\mathcal{O}(h^4)$. For the OPS method, this is simply

$$\frac{\partial\ell}{\partial\theta_i} \approx \frac{-\ell(\hat{\theta}+2he_i) + 8\ell(\hat{\theta}+he_i) - 8\ell(\hat{\theta}-he_i) + \ell(\hat{\theta}-2he_i)}{12h} + \mathcal{O}(h^4) \tag{5}$$

followed by summing the contributions of the log-likelihood at each site according to Eq. (2). Regarding the direct second-order derivative method, the result is more complex and is detailed in Note S3.3.

In phyloHessian, the default algorithm is the OPS method, which is employed by CODEML in PAML v4.3+. Alternatively, users can specify the second-order derivative method, as used in PAML 4.1 and earlier versions. Users can also specify the order of the error term, allowing balancing computational accuracy with speed based on their needs.

Simulation procedure

We evaluated the performance of different substitution models using simulated data that mimics deep-time evolution (Fig. S16). In our focal simulation scheme, for each substitution model used in sequence evolution simulation (details provided below), we generated 30 timetrees each with

530 20 tips, using the R package TreeSim (Stadler 2011). Following our previous work (Wang and
531 Luo 2025), timetrees were created under a birth-death model with birth and death rates of 0.4 and
532 0.2 lineages per 0.1 Gyr as estimated in a prior study of prokaryotic lineage diversification
533 (Scholl and Wiens 2016), and with a taxon sampling proportion of 10% (see Note S1 for
534 alternative settings). Simulated trees were generated with true root ages of 1.0, 2.0, 3.0, and 4.0
535 Ga to represent a range of evolutionary timescales approaching the age of Earth (~4.5 Ga).
536 For each timetree, branch-specific substitution rates were sampled under both the
537 independent rates (IR) and autocorrelated rates (AR) model. For the IR mode, following our
538 previous study (Wang and Luo 2021), the rate follows lognormal distribution with parameters
539 $\mu_{\mathrm{IR}} = -3.7$ and $\sigma_{\mathrm{IR}} = 0.2$, such that the mean of rate is $\mathrm{e}^{\mu_{\mathrm{IR}}+\frac{\sigma_{\mathrm{IR}}^2}{2}} \approx 0.025$ substitutions/site/0.1
540 Gyr, with a standard deviation of $\sqrt{\left(e^{\sigma_{\mathrm{IR}}^2}-1\right)e^{\left(2\mu_{\mathrm{IR}}+\sigma_{\mathrm{IR}}^2\right)}} \approx 0.005$ substitutions/site/0.1 Gyr. This
541 roughly corresponds to empirical observations that tip-to-root distances in the bacterial tree of
542 life, constructed with universally conserved orthologs, are roughly 1.0 amino acid
543 substitutions/site (Moody et al. 2022; Wang and Luo 2025), assuming an origin of early life at
544 around 4.0 Ga (Battistuzzi and Hedges 2009; Marin et al. 2017; Betts et al. 2018; Moody et al.
545 2024). The methodology used to determine the simulation parameters for the AR model is
546 described in detail in the next section.
547 Alignments of 300 amino acids (aa) were simulated using AliSim (Ly-Trong et al. 2022)
548 according to the timetree generated by simulation, under various substitution models. In the focal
549 analysis, we employed the LG+C60+G4{1.0} model. This indicates LG substitution model plus
550 C60 profile mixture models (60 empirically derived amino acid site frequency profiles) (Quang
551 et al. 2008) and across-site rate variation under a discrete gamma distribution with four relative
552 rate categories parameterized by $\alpha = 1.0$, hence Gamma(1,1), meaning that the mean and

variance of the across-site relative rates are $\frac{1}{1} = 1$ and $\frac{1}{1^2} = 1$ respectively (Yang 1994). Further, we varied several simulation parameters, including sequence length, number of taxa, calibration strategies, birth-death process parameters, across-site rate heterogeneity, molecular clock settings, and model misspecifications. These are detailed in Note S1.

Determining the parameters for simulation under the AR clock rate model

Denote the absolute rate of sequence evolution (measured in substitutions per site per time unit) under IR and AR respectively as the vectors $X_{\mathrm{IR}} = \left(X_{1,\mathrm{IR}}, \dots, X_{n,\mathrm{IR}}\right)$ and $X_{\mathrm{AR}} = \left(X_{1,\mathrm{AR}}, \dots, X_{n,\mathrm{AR}}\right)$ where n represents the number of branches. Their log-transformed values are given by $Y_{\mathrm{IR}} = (Y_{1,\mathrm{IR}}, \dots, Y_{n,\mathrm{IR}})$ and $Y_{\mathrm{AR}} = (Y_{1,\mathrm{AR}}, \dots, Y_{n,\mathrm{AR}})$. To make simulations under IR and AR models more comparable, we require that the expectations of the sample mean and sample variance of the log-transformed rate under the two models to be equal, respectively, given the same phylogeny. Mathematically, this requires that

$$\mathrm{E}(\bar{Y}_{\mathrm{AR}}) = \mathrm{E}(\bar{Y}_{\mathrm{IR}}), \quad \mathrm{E}(s^2_{\mathrm{AR}}) = \mathrm{E}(s^2_{\mathrm{IR}}) \tag{6}$$

where the sample variances of the log-transformed rates are denoted by s^2_{AR} and s^2_{IR}.

For the IR model, it is assumed that the rate for each branch, denoted $X_{\mathrm{IR}} = \left[X_{1,\mathrm{IR}}, \dots, X_{n,\mathrm{IR}}\right]$, is independently and identically (*i.i.d.*) distributed according to a lognormal distribution with parameters μ_{IR} and σ^2_{IR}, such that the rate for each branch can be expressed as $X_{i,\mathrm{IR}} \sim \mathrm{Lognormal}(\mu_{\mathrm{IR}}, \sigma^2_{\mathrm{IR}})$. In other words, we have

$$\mathrm{E}(\bar{Y}_{\mathrm{IR}}) = \mu_{\mathrm{IR}}, \quad \mathrm{E}(s^2_{\mathrm{IR}}) = \sigma^2_{\mathrm{IR}}. \tag{7}$$

The AR model in molecular clock dating, also known as the geometric Brownian (GBM) model, assumes that the lineage-specific rate follows a geometric Brownian motion with a drift parameter of zero. It is thus parameterized by two parameters, μ_{AR}, the log-transformed rate at

the root, and σ^2_{AR}, which determines the volatility of the rate changes over time. Accordingly, it can be shown that the log-transformed rate under AR model after time t follows $\mathcal{N}\left(\mu_{\mathrm{AR}} - \frac{1}{2}t\sigma^2_{\mathrm{AR}}, t\sigma^2_{\mathrm{AR}}\right)$ (Rannala and Yang 2007; Panchaksaram et al. 2025). Denote $C = \left[c_{ij}\right]_{n\times n}$ the branch-wise covariance matrix where n is the number of branches in a rooted tree (note that this is different from what is so-called phylogenetic covariance matrix which is related to only the tips [Fig. S17]). Further, the log-transformed rates Y_{AR} follow the following multivariate distribution

$$Y_{\mathrm{AR}} \sim \mathcal{N}\left(\left(\mu_{\mathrm{AR}} - \frac{1}{2}\sigma^2_{\mathrm{AR}}c_{11}, \ldots, \mu_{\mathrm{AR}} - \frac{1}{2}\sigma^2_{\mathrm{AR}}c_{nn}\right), \sigma^2_{\mathrm{AR}}C\right).$$

Thus, it is easy to see that

$$\mathrm{E}\left(Y_{i,\mathrm{AR}}\right) = \mu_{\mathrm{AR}} - \frac{1}{2}\sigma^2_{\mathrm{AR}}c_{ii}. \tag{8}$$

The expectation of the sample variance s^2_{AR} of log-transformed rate Y_{AR} across all n branches is calculated as

$$\mathrm{E}(s^2_{AR}) = \frac{1}{n-1}\mathrm{E}\left(\sum\nolimits_{i=1}\left(Y_{i,\mathrm{AR}} - \frac{1}{n}\sum\nolimits_{j=1} Y_{j,\mathrm{AR}}\right)^2\right). \tag{9}$$

Expanding the right-hand side, we obtain

$$\mathrm{E}\left[\sum_{i=1}^{n}\left(Y_{i,\mathrm{AR}} - \frac{1}{n}\sum_{j=1}^{n} Y_{j,\mathrm{AR}}\right)^2\right]$$

$$= \sum_{i=1}^{n}\mathrm{E}\left(Y^2_{i,\mathrm{AR}}\right) - \frac{1}{n}\sum_{i=1}^{n}\left(\sum_{j=1}^{n} 2\mathrm{E}\left(Y_{i,\mathrm{AR}}Y_{j,\mathrm{AR}}\right) - \frac{1}{n}\sum_{j=1}^{n}\sum_{k=1}^{n}\mathrm{E}\left(Y_{j,\mathrm{AR}}Y_{k,\mathrm{AR}}\right)\right)$$

$$= \sum_{i=1}^{n} \mathrm{E}\left(Y_{i,\mathrm{AR}}^2\right) - \frac{1}{n}\sum_{i=1}^{n}\sum_{j=1}^{n} \mathrm{E}\left(Y_{i,\mathrm{AR}}Y_{j,\mathrm{AR}}\right). \tag{10}$$

Further, note the following relationship

$$\mathrm{E}\left(Y_{i,\mathrm{AR}}^2\right) = \mathrm{Var}\left(Y_{i,\mathrm{AR}}\right) + \left[\mathrm{E}\left(Y_{i,\mathrm{AR}}\right)\right]^2 = c_{ii}\sigma_{\mathrm{AR}}^2 + \left(\mu_{\mathrm{AR}} - \frac{1}{2}\sigma_{\mathrm{AR}}^2 c_{ii}\right)^2,$$

$$\mathrm{E}\left(Y_{i,\mathrm{AR}}Y_{j,\mathrm{AR}}\right) = \mathrm{Cov}\left(Y_{i,\mathrm{AR}}, Y_{j,\mathrm{AR}}\right) + \mathrm{E}\left(Y_{i,\mathrm{AR}}\right)\mathrm{E}\left(Y_{j,\mathrm{AR}}\right)$$

$$= \sigma_{\mathrm{AR}}^2 c_{ij} + \left(\mu_{\mathrm{AR}} - \frac{1}{2}\sigma_{\mathrm{AR}}^2 c_{ii}\right)\left(\mu_{\mathrm{AR}} - \frac{1}{2}\sigma_{\mathrm{AR}}^2 c_{jj}\right).$$

Introducing the above into Eq. (10), we have

$$\sum_{i=1}^{n} \mathrm{E}\left(Y_{i,\mathrm{AR}}^2\right) - \frac{1}{n}\sum_{i=1}^{n}\sum_{j=1}^{n} \mathrm{E}\left(Y_{i,\mathrm{AR}}Y_{j,\mathrm{AR}}\right)$$

$$= \sum\nolimits_i \left[c_{ii}\sigma_{\mathrm{AR}}^2 + \left(\mu_{\mathrm{AR}} - \frac{1}{2}c_{ii}\sigma_{\mathrm{AR}}^2\right)^2\right] - \frac{1}{n}\sum\nolimits_{i,j}\left[c_{ij}\sigma_{\mathrm{AR}}^2 + \left(\mu_{\mathrm{AR}} - \frac{1}{2}c_{ii}\sigma_{\mathrm{AR}}^2\right)\left(\mu_{\mathrm{AR}} - \frac{1}{2}c_{jj}\sigma_{\mathrm{AR}}^2\right)\right]$$

$$= \underbrace{\sigma_{\mathrm{AR}}^2\left[\sum\nolimits_i c_{ii} - \frac{1}{n}\sum\nolimits_{i,j} c_{ij}\right]}_{\text{Term 1}}$$

$$+ \underbrace{\left[\sum\nolimits_i \left(\mu_{\mathrm{AR}} - \frac{1}{2}c_{ii}\sigma_{\mathrm{AR}}^2\right)^2 - \frac{1}{n}\sum\nolimits_{i,j}\left(\mu_{\mathrm{AR}} - \frac{1}{2}c_{ii}\sigma_{\mathrm{AR}}^2\right)\left(\mu_{\mathrm{AR}} - \frac{1}{2}c_{jj}\sigma_{\mathrm{AR}}^2\right)\right]}_{\text{Term 2}}$$

Substituting $\sum_{\mathrm{i}} c_{ii} = \mathrm{tr}(C)$ and $\sum_{i,j} c_{ij} = \frac{1}{n}\mathbf{1}'C\mathbf{1}$ into Term 1, we can rewrite it as

$$\sigma_{\mathrm{AR}}^2\left[\sum\nolimits_i c_{ii} - \frac{1}{n}\sum\nolimits_{i,j} c_{ij}\right] = \sigma_{\mathrm{AR}}^2\left[\mathrm{tr}(C) - \frac{1}{n}\mathbf{1}'C\mathbf{1}\right].$$

For Term 2, noting that terms involving μ_{AR} cancels out, we have

$$\sum\nolimits_i \left(\mu_{\mathrm{AR}} - \frac{1}{2}c_{ii}\sigma_{\mathrm{AR}}^2\right)^2 - \frac{1}{n}\sum\nolimits_{i,j}\left(\mu_{\mathrm{AR}} - \frac{1}{2}c_{ii}\sigma_{\mathrm{AR}}^2\right)\left(\mu_{\mathrm{AR}} - \frac{1}{2}c_{jj}\sigma_{\mathrm{AR}}^2\right)$$

$$= \left(n\mu_{\mathrm{AR}}^2 - \mu_{\mathrm{AR}}\sigma_{\mathrm{AR}}^2\mathrm{tr}(C) + \frac{1}{4}\sum\nolimits_i c_{ii}^2\sigma_{\mathrm{AR}}^4\right) + \left(-n\mu_{\mathrm{AR}}^2 + \mu_{\mathrm{AR}}\sigma_{\mathrm{AR}}^2\mathrm{tr}(C) - \frac{1}{4n}\sum\nolimits_{i,j} c_{ii}c_{jj}\sigma_{\mathrm{AR}}^4\right)$$

$$= \frac{\sigma_{\mathrm{AR}}^4}{4}\left[\sum_i c_{ii}^2 - \frac{1}{n}\left(\mathrm{tr}(C)\right)^2\right].$$

Hence,

$$\mathrm{E}(s_{\mathrm{AR}}^2) = \frac{\sigma_{\mathrm{AR}}^2}{n-1}\left[\left(\mathrm{tr}(C) - \frac{1}{n}\mathbf{1}'C\mathbf{1}\right) + \frac{\sigma_{\mathrm{AR}}^2}{4}\left(\sum_i c_{ii}^2 - \frac{1}{n}\left(\mathrm{tr}(C)\right)^2\right)\right].$$

Because $\mathrm{E}(s_{\mathrm{IR}}^2) = \sigma_{\mathrm{IR}}^2$, equating $\mathrm{E}(s_{\mathrm{IR}}^2)$ with $\mathrm{E}(s_{\mathrm{AR}}^2)$ and rearranging terms yields the quadratic equation for σ_{AR}^2

$$\frac{1}{4}\left[\sum_i c_{ii}^2 - \frac{1}{n}\left(\mathrm{tr}(C)\right)^2\right]\sigma_{\mathrm{AR}}^4 + \left[\mathrm{tr}(C) - \frac{1}{n}\mathbf{1}'C\mathbf{1}\right]\sigma_{\mathrm{AR}}^2 - (n-1)\sigma_{\mathrm{IR}}^2 = 0. \qquad (11)$$

Discarding the negative root, along with solving Eq. (8), we ultimately get

$$\hat{\sigma}_{\mathrm{AR}}^2 = \frac{2(n-1)\sigma_{\mathrm{IR}}^2}{\sqrt{a^2 + 4b(n-1)\sigma_{\mathrm{IR}}^2} + a}, \quad \hat{\mu}_{\mathrm{AR}} = \mu_{\mathrm{IR}} - \frac{\hat{\sigma}_{\mathrm{AR}}^2 \mathrm{tr}(C)}{2n} \qquad (12)$$

where $a = \mathrm{tr}(C) - \frac{1}{n}\mathbf{1}'C\mathbf{1}$, $b = \frac{1}{4}\left[\sum_i c_{ii}^2 - \frac{1}{n}\left(\mathrm{tr}(C)\right)^2\right]$, and $\hat{\sigma}_{\mathrm{AR}}^2$ and $\hat{\mu}_{\mathrm{AR}}$ are the values of the parameters for the AR model that satisfy Eq. (6) given the parameters for the IR model (σ_{IR}^2 and μ_{IR}).

Calibrations used in molecular dating analysis on simulated datasets

Molecular dating analysis were conducted using MCMCtree v4.10.7 (see also Note S3) on phylogenies simulated with procedures described above under varying calibration strategies: a root-only calibration, or root calibration plus one internal calibration, chosen as the node at the median age of all nodes in the true timetree, or two internal calibrations which targeted the 1/3 and 2/3 age quantiles. Time priors for calibrated nodes were set to be uniform within the interval [true_age - (true_age/5), true_age + (true_age/5)], with soft bounds (MCMCtree's default: 2.5% probability of age outside bounds). Other information about MCMCtree analysis can be found in

628 Note S3. The five calibration schemes mainly used in the present study are *root_only*: a single
629 bounded calibration (both upper and lower bounds); *one_min*: bounded calibration at the root
630 and one minimum-bounded internal node; *single_interval*: bounded calibration at both the root
631 and an internal node; *two_min*: bounded calibration at the root and two minimum-bounded
632 internal nodes; *two_intervals*: bounded calibration at both the root and two internal nodes.
633

634 **Comparing the performance of different substitution models on simulated datasets**

635 We evaluated the performance of various substitution models mainly using the relative difference
636 (reldiff) that compared the posterior mean divergence times and substitution rates estimated by
637 MCMCtree (using each model) to the true values used in simulations. Relative difference:
638 calculated as $mean\left(\frac{|b_i^m - b_i^{true}|}{\max(b_i^m, b_i^{true})}\right)$, where b_i^m and b_i^{true} denote the posterior mean divergence
639 times or branch-specific substitution rates inferred by MCMCtree, and those used in simulation
640 (true values), respectively.
641

642 **Empirical data analysis**

643 Genomes of Microsporidia and Rickettsiales were downloaded from MicrosporadiaDB
644 (Aurrecoechea et al. 2011) and GenBank (last accessed July 2024), respectively. Sequences of
645 five additional Proteobacteria as the outgroup were retrieved from our prior study (Wang and
646 Luo 2025). TreeCluster v1.0.4 (Balaban et al. 2019) was used to select representative taxa with a
647 cutoff of phylogenetic depth (which take phylogenetic distance and topology into account to
648 cluster taxa into subclades) of 0.5 and 2.5 respectively for Microsporidia (yielding 27 members)
649 and Rickettsiales (22 members). Genes used to reconstruct phylogeny and molecular dating for
650 Microsporidia were based on 27 orthologs identified by OrthoFinder v3.0.1 (Emms and Kelly

2019) present in all members allowing ≤2 copies per genome, while for Rickettsiales we adopted the mitochondrial endosymbiosis-based strategy (Wang and Luo 2021) by using 24 mitochondria-encoded genes conserved across Alphaproteobacteria (Wang and Wu 2015) (see Data availability). For both datasets, we partitioned the alignments into one, two, or three subsets by fitting the logarithm of the average substitution rates estimated by CODEML into a Gaussian mixture model. We selected the best-fitting substitution models for each partition under both site-homogeneous and site-heterogeneous models according to AIC (Note S3). Calibration information along with alternatives is available in Data S6.

Data availability

phyloHessian is available at https://github.com/evolbeginner/phyloHessianWrapper. Other codes and the scripts (Goto et al. 2010) generating them, are made available at https://figshare.com/s/96bc117f18051f9642ce.

Acknowledgements

We thank Mario dos Reis, Xiyun Jiao, Jianhao Lv, Gergely Szöllősi, Ziheng Yang, and Tianqi Zhu for discussion. We also thank Bui Quang Minh for kindly sharing with us their manuscript, and Margaret Ip and Haiwei Luo for their support. The work is supported by Hong Kong Research Grants Council (RGC) General Research Fund (GRF) (14112024), Natural Science Foundation of China (32400493, 42293294), and CUHK Direct Grant (4054912).

672 **References**

673 Aurrecoechea C, Barreto A, Brestelli J, Brunk BP, Caler EV, Fischer S, Gajria B, Gao X, Gingle
674 A, Grant G, et al. 2011. AmoebaDB and MicrosporidiaDB: functional genomic resources
675 for Amoebozoa and Microsporidia species. *Nucleic Acids Res.* 39:D612-619.

676 Balaban M, Moshiri N, Mai U, Jia X, Mirarab S. 2019. TreeCluster: Clustering biological
677 sequences using phylogenetic trees. *PLoS ONE* 14:e0221068.

678 Baños H, Susko E, Roger AJ. 2024. Is Over-parameterization a Problem for Profile Mixture
679 Models? *Syst. Biol.* 73:53–75.

680 Baños H, Wong TKF, Daneau J, Susko E, Minh BQ, Lanfear R, Brown MW, Eme L, Roger AJ.
681 2024. GTRpmix: A Linked General Time-Reversible Model for Profile Mixture Models.
682 *Mol. Biol. Evol.* 41:msae174.

683 Battistuzzi FU, Hedges SB. 2009. A Major Clade of Prokaryotes with Ancient Adaptations to
684 Life on Land. *Mol. Biol. Evol.* 26:335–343.

685 Betts HC, Puttick MN, Clark JW, Williams TA, Donoghue PCJ, Pisani D. 2018. Integrated
686 genomic and fossil evidence illuminates life's early evolution and eukaryote origin. *Nat.*
687 *Ecol. Evol.* 2:1556–1562.

688 Bujaki T, Rodrigue N. 2022. Bayesian Cross-Validation Comparison of Amino Acid
689 Replacement Models: Contrasting Profile Mixtures, Pairwise Exchangeabilities, and
690 Gamma-Distributed Rates-Across-Sites. *J. Mol. Evol.* 90:468–475.

691 Capella-Gutiérrez S, Marcet-Houben M, Gabaldón T. 2012. Phylogenomics supports
692 microsporidia as the earliest diverging clade of sequenced fungi. *BMC Biol.* 10:47.

693 Castelli M, Nardi T, Gammuto L, Bellinzona G, Sabaneyeva E, Potekhin A, Serra V, Petroni G,
694 Sassera D. 2024. Host association and intracellularity evolved multiple times
695 independently in the Rickettsiales. *Nat. Commun.* 15.

696 Castelli M, Sassera D, Petroni G. 2016. Biodiversity of "non-model" Rickettsiales and their
697 association with aquatic organisms. In: Rickettsiales: Biology, Molecular Biology,
698 Epidemiology, and Vaccine Development. p. 59–91.

699 Demotte P, Panchaksaram M, Kumarasinghe H, Ly-Trong N, Reis M dos, Minh BQ. 2025.
700 IQ2MC: A New Framework to Infer Phylogenetic Time Trees Using IQ-TREE 3 and
701 MCMCTree with Mixture Models. Available from:
702 https://ecoevorxiv.org/repository/view/9125/

703 Drummond AJ, Ho SYW, Phillips MJ, Rambaut A. 2006. Relaxed phylogenetics and dating with
704 confidence. *PLoS Biol.* 4:699–710.

705 Emms DM, Kelly S. 2019. OrthoFinder: Phylogenetic orthology inference for comparative
706 genomics. *Genome Biol.* 20:238.

Gaston D, Susko E, Roger AJ. 2011. A phylogenetic mixture model for the identification of functionally divergent protein residues. *Bioinformatics* 27:2655–2663.

Goto N, Prins P, Nakao M, Bonnal R, Aerts J, Katayama T. 2010. BioRuby: Bioinformatics software for the Ruby programming language. *Bioinformatics* 26:2617–2619.

Guindon S. 2019. PhyML Manual. Available from: https://gensoft.pasteur.fr/docs/phyml/3.3.20190909/phyml-manual.pdf

Guindon S. 2020. Rates and Rocks: Strengths and Weaknesses of Molecular Dating Methods. *Front. Genet.* [Internet] 11. Available from: https://www.frontiersin.org/journals/genetics/articles/10.3389/fgene.2020.00526/full

Guindon S, Dufayard JF, Lefort V, Anisimova M, Hordijk W, Gascuel O. 2010. New algorithms and methods to estimate maximum-likelihood phylogenies: Assessing the performance of PhyML 3.0. *Syst. Biol.* 59:307–321.

Ho SYW, Duchêne S. 2014. Molecular-clock methods for estimating evolutionary rates and timescales. *Mol. Ecol.* 23:5947–5965.

Lartillot N, Brinkmann H, Philippe H. 2007. Suppression of long-branch attraction artefacts in the animal phylogeny using a site-heterogeneous model. *BMC Evol. Biol.* 7:S4.

Lartillot N, Philippe H. 2004. A Bayesian Mixture Model for Across-Site Heterogeneities in the Amino-Acid Replacement Process. *Mol. Biol. Evol.* 21:1095–1109.

Le SQ, Dang CC, Gascuel O. 2012. Modeling protein evolution with several amino acid replacement matrices depending on site rates. *Mol. Biol. Evol.* 29:2921–2936.

Le SQ, Gascuel O. 2008. An improved general amino acid replacement matrix. *Mol. Biol. Evol.* 25:1307–1320.

Le SQ, Gascuel O. 2010. Accounting for Solvent Accessibility and Secondary Structure in Protein Phylogenetics Is Clearly Beneficial. *Syst. Biol.* 59:277–287.

Le SQ, Lartillot N, Gascuel O. 2008. Phylogenetic mixture models for proteins. *Philos. Trans. R. Soc. B Biol. Sci.* 363:3965–3976.

Ly-Trong N, Naser-Khdour S, Lanfear R, Minh BQ. 2022. AliSim: A Fast and Versatile Phylogenetic Sequence Simulator for the Genomic Era. *Mol. Biol. Evol.* [Internet] 39. Available from: https://doi.org/10.1093/molbev/msac092

Mahendrarajah TA, Moody ERR, Schrempf D, Szánthó LL, Dombrowski N, Davín AA, Pisani D, Donoghue PCJ, Szöllősi GJ, Williams TA, et al. 2023. ATP synthase evolution on a cross-braced dated tree of life. *Nat. Commun.* 14:7456.

Marin J, Battistuzzi FU, Brown AC, Hedges SB. 2017. The Timetree of Prokaryotes: New Insights into Their Evolution and Speciation. *Mol. Biol. Evol.* 34:437–446.

Martijn J, Vosseberg J, Guy L, Offre P, Ettema TJG. 2018. Deep mitochondrial origin outside the sampled alphaproteobacteria. *Nature* 557:101–105.

Moody ERR, Álvarez-Carretero S, Mahendrarajah TA, Clark JW, Betts HC, Dombrowski N, Szánthó LL, Boyle RA, Daines S, Chen X, et al. 2024. The nature of the last universal common ancestor and its impact on the early Earth system. *Nat. Ecol. Evol.* 8:1654–1666.

Moody ERR, Mahendrarajah TA, Dombrowski N, Clark JW, Petitjean C, Offre P, Szöllősi GJ, Spang A, Williams TA. 2022. An estimate of the deepest branches of the tree of life from ancient vertically evolving genes. *eLife* 11.

Pagel M, Meade A. 2004. A phylogenetic mixture model for detecting pattern-heterogeneity in gene sequence or character-state data. *Syst. Biol.* 53:571–581.

Panchaksaram M, Freitas L, Dos Reis M. 2025. Bayesian Selection of Relaxed-Clock Models: Distinguishing between Independent and Autocorrelated Rates. *Syst. Biol.* 74:323–334.

Parfrey LW, Lahr DJG, Knoll AH, Katz LA. 2011. Estimating the timing of early eukaryotic diversification with multigene molecular clocks. *Proc. Natl. Acad. Sci. U. S. A.* 108:13624–13629.

Pawitan Y. 2001. In all likelihood: statistical modelling and inference using likelihood. Oxford University Press

Quang LS, Gascuel O, Lartillot N. 2008. Empirical profile mixture models for phylogenetic reconstruction. *Bioinformatics* 24:2317–2323.

Rannala B, Yang Z. 2007. Inferring speciation tunes under an episodic molecular clock. *Syst. Biol.* 56:453–466.

dos Reis M, Donoghue PCJ, Yang Z. 2016. Bayesian molecular clock dating of species divergences in the genomics era. *Nat. Rev. Genet.* 17:71–80.

dos Reis M, Yang Z. 2011. Approximate likelihood calculation on a phylogeny for Bayesian Estimation of Divergence Times. *Mol. Biol. Evol.* 28:2161–2172.

Scholl JP, Wiens JJ. 2016. Diversification rates and species richness across the Tree of Life. *Proc. R. Soc. B Biol. Sci.* 283:20161335.

Schrempf D, Lartillot N, Szöllosi G. 2020. Scalable empirical mixture models that account for across-site compositional heterogeneity. *Mol. Biol. Evol.* 37:3616–3631.

Seo TK, Kishino H, Thorne JL. 2004. Estimating absolute rates of synonymous and nonsynonymous nucleotide substitution in order to characterize natural selection and date species divergences. *Mol. Biol. Evol.* 21:1201–1213.

Stadler T. 2011. Simulating trees with a fixed number of extant species. *Syst. Biol.* 60:676–684.

774 Szánthó LL, Lartillot N, Szöllősi GJ, Schrempf D. 2023. Compositionally Constrained Sites
775 Drive Long-Branch Attraction. *Syst. Biol.* 72:767–780.

776 Thorne JL, Kishino H, Painter IS. 1998. Estimating the rate of evolution of the rate of molecular
777 evolution. *Mol. Biol. Evol.* 15:1647–1657.

778 Venditti C, Meade A, Pagel M. 2008. Phylogenetic Mixture Models Can Reduce Node-Density
779 Artifacts. *Syst. Biol.* 57:286–293.

780 Wang HC, Li K, Susko E, Roger AJ. 2008. A class frequency mixture model that adjusts for site-
781 specific amino acid frequencies and improves inference of protein phylogeny. *BMC Evol.*
782 *Biol.* 8.

783 Wang HC, Minh BQ, Susko E, Roger AJ. 2018. Modeling Site Heterogeneity with Posterior
784 Mean Site Frequency Profiles Accelerates Accurate Phylogenomic Estimation. *Syst. Biol.*
785 67:216–235.

786 Wang HC, Susko E, Roger AJ. 2019. The Relative Importance of Modeling Site Pattern
787 Heterogeneity Versus Partition-Wise Heterotachy in Phylogenomic Inference. *Syst. Biol.*
788 68:1003–1019.

789 Wang S, Luo H. 2021. Dating Alphaproteobacteria evolution with eukaryotic fossils. *Nat.*
790 *Commun.* 12:3324.

791 Wang S, Luo H. 2025. Dating the bacterial tree of life based on ancient symbiosis. *Syst.*
792 *Biol.*:syae071.

793 Wang Z, Wu M. 2015. An integrated phylogenomic approach toward pinpointing the origin of
794 mitochondria. *Sci. Rep.* 5:7949.

795 Williams TA, Cox CJ, Foster PG, Szöllősi GJ, Embley TM. 2020. Phylogenomics provides
796 robust support for a two-domains tree of life. *Nat. Ecol. Evol.* 4:138–147.

797 Wong TKF, Ly-Trong N, Ren H, Baños H, Roger AJ, Susko E, Bielow C, Maio ND, Goldman N,
798 Hahn MW, et al. 2025. IQ-TREE 3: Phylogenomic Inference Software using Complex
799 Evolutionary Models. Available from: https://ecoevorxiv.org/repository/view/8916/

800 Yang Z. 1993. Maximum-likelihood estimation of phylogeny from DNA sequences when
801 substitution rates differ over sites. *Mol. Biol. Evol.* 10:1396–1401.

802 Yang Z. 1994. Maximum likelihood phylogenetic estimation from DNA sequences with variable
803 rates over sites: Approximate methods. *J. Mol. Evol.* 39:306–314.

804 Yang Z, Rannala B. 2006. Bayesian estimation of species divergence times under a molecular
805 clock using multiple fossil calibrations with soft bounds. *Mol. Biol. Evol.* 23:212–226.

806 Zuckerkandl E, Pauling L. 1965. Evolutionary Divergence and Convergence in Proteins. In:
807 Evolving Genes and Proteins. p. 97–166.

808

809

810

811 **Figure legends**

812 **Figure 1.** Comparison of the accuracy of divergence time (A) and branch-specific substitution
813 rate (B) estimation under substitution models LG+G and LG+C60+G by simulation. Each plot
814 contains 30 dots representing the mean relative difference (compared to the true values used in
815 simulation) based on MCMCtree molecular clock dating with the corresponding calibration
816 strategy on 30 simulated datasets. For each simulation, 30 timetrees each containing 20 tips are
817 simulated using a birth-death process with a mean substitution rate 0.25 substitutions/site/Gyr
818 across four different root ages ranging from 1.0 to 4.0 Ga. Sequence alignments are generated
819 with LG+C60+G4{1.0} (+G4{1.0} indicates $\alpha = 1$ in a four-category discrete Gamma-
820 distributed across-site relative rates) under AR (left-hand side) and IR (right-hand side) clock
821 models respectively. *P*-values are obtained from a paired Wilcoxon signed-rank test. The box
822 plots (median, interquartile range, 1.5×IQR whiskers) illustrate the relative differences in time
823 (A) and rate (B) estimates compared to true values. (C) A schematic figure showing the five
824 calibration schemes used for molecular clock analyses on simulated data. *root_only*: a single
825 bounded calibration (both upper and lower bounds); *one_min*: bounded calibration at the root
826 and one minimum-bounded internal node; *single_interval*: bounded calibration at both the root
827 and an internal node; *two_min*: bounded calibration at the root and two minimum-bounded
828 internal nodes; *two_intervals*: bounded calibration at both the root and two internal nodes.

829

830 **Figure 2.** Investigating the robustness of divergence time estimation to alternative settings in
831 simulation. (A) Sequence simulated under substitution model LG+C60+G4{0.5} (*Gamma_0.5*;
832 the parameter alpha in the discrete Gamma distribution equal to 0.5), thus more rate
833 heterogeneity across sites than the focal analysis (LG+C60+G4{1.0}). (B) Timetree simulated

834 under a flat time prior (*bd_flat*). (C) Timetree simulated under a molecular clock with larger
835 across-branch rate variance (*sigma_0.38*). The plots on the left and right correspond to analyses
836 using the AR and IR clock models, respectively. More detailed information about the above
837 alternative simulation schemes can be found in Note S1. Calibration strategies and other settings
838 are the same as those used in Fig. 1.
839
840 **Figure 3**. Evaluation of the impacts of calibration and model misspecification on molecular
841 clock dating. Accuracy of divergence time estimation (relative difference) is shown as the *y*-axis.
842 (A, B) The lower and upper time bounds of all calibrations are shifted forward (A) and backward
843 (B) in time by 20% of their true values, respectively. (C) Assessment of the accuracy of
844 divergence time estimation under alternative substitution models used in simulation (LG+C60+G
845 used in most other analyses): LG+G, LG+G+I, LG+R, LG+C20+G, LG+C60+G+I. Boxplots
846 compare the accuracy obtained by the true model (red) and by LG+C60+G (light green). Each
847 plot contains 30 dots representing the mean relative difference based on MCMCtree molecular
848 clock dating with the corresponding calibration strategy on 30 simulated datasets. For each
849 simulation, 30 timetrees each containing 20 tips are simulated using a birth-death process with a
850 mean substitution rate 0.25 substitutions/site/Gyr across four different root ages ranging from 1.0
851 to 4.0 Ga. The plots on the left and right correspond to analyses using the AR and IR clock
852 models, respectively. Calibration strategies are the same as those used in Fig. 1.
853
854 **Figure 4**. Evaluation of the approximation of PMSF and bootstrapped Hessian on molecular
855 clock analysis by simulation. Phylogenies are simulated under the same strategy as the focal
856 dataset. The sequence alignment is simulated under LG+C60+G{1.0}. The bootstrapped Hessian

857 matrix is calculated using the software bs_inBV. The *y*-axis indicates the relative accuracy of the
858 posterior mean of the divergence times (A) or substitution rates (B) compared to that obtained by
859 the first MCMC run under LG+C60+G (note that this is different from other figures where the
860 baseline in comparison is the true simulated times and rates). Each plot contains 30 dots
861 representing the mean relative difference based on MCMCtree molecular clock dating with the
862 corresponding calibration strategy on 30 simulated datasets. For each simulation, 30 timetrees
863 each containing 20 tips are simulated using a birth-death process with a mean substitution rate
864 0.25 substitutions/site/Gyr across four different root ages ranging from 1.0 to 4.0 Ga.
865 *LG+C60+G_run2*: the second independent MCMC run of MCMCtree under LG+C60+G.
866 *LG+C60+G+PMSF*: PMSF approximation with LG+C60+G. *LG+C60+G+bs_inBV*:
867 bootstrapped Hessian under LG+C60+G. *LG+C60+G+PMSF+bs_inBV:* bootstrapped Hessian
868 under LG+C60+G+PMSF. Calibration strategies are the same as those used in Fig. 1.
869
870 **Figure 5.** Evolutionary timeline and substitution rates estimated by MCMCtree under different
871 substitution models for Microsporidia. A uniform calibration prior between 0.5 and 0.9 Ga was
872 applied to the root (see Note S2), with soft bounds extending 2.5% beyond each time bound.
873 Branch colors indicate the logarithm of the posterior mean substitution rate (estimated by
874 MCMCtree), ranging from blue (low) to red (high). (B) Posterior divergence times and branch-
875 specific substitution rates estimated by the mixture substitution model (*y*-axis) versus those
876 estimated by the homogeneous substitution model (*x*-axis) under the AR or IR clock models. The
877 bars indicate the 95% HPD.
878

879 **Figure 6.** Evolutionary timeline and substitution rates estimated by MCMCtree under different
880 substitution models for Rickettsiales. This is based the mitochondrial endosymbiosis dating
881 strategy (Wang and Luo 2021), using eukaryotic fossils to calibrate Rickettsiales evolution,
882 based on the evolutionary scenario that mitochondria originated from a lineage closely related to
883 α-Proteobacteria. (A) The estimated evolutionary timeline of Rickettsiales under different
884 substitution (the best-fitting homogeneous or mixture) and clock (IR or AR) models. All
885 calibrated nodes are denoted by a circle. In addition to the calibration at the root, all four
886 calibrations are placed within eukaryotes in the clade of mitochondria (see Note S2). Branch
887 colors indicate the logarithm of the posterior mean substitution rate estimated by MCMCtree,
888 ranging from blue (low) to red (high). (B) Posterior divergence times and branch-specific
889 substitution rates estimated by the mixture substitution model (*y*-axis) versus those estimated by
890 the homogeneous substitution model (*x*-axis) under the AR or IR clock models. The bars indicate
891 the 95% HPD.
892
893

Table 1. Reduction of the relative differences in substitution rate estimates, calculated as as $\frac{\text{reldiff}_{\text{LG+G}} - \text{reldiff}_{\text{LG+C60+G}}}{\text{reldiff}_{\text{LG+G}}}$, under LG+G versus LG+C60+G under different root ages and calibration strategies.

Calibration strategy	**AR (root age)**				**IR (root age)**			
	1.0 Ga	2.0 Ga	3.0 Ga	4.0 Ga	1.0 Ga	2.0 Ga	3.0 Ga	4.0 Ga
root_only	26%	35%	47%	51%	23%	44%	52%	55%
one_min	27%	38%	53%	56%	24%	46%	52%	59%
single_interval	23%	41%	51%	55%	24%	44%	49%	55%
two_min	28%	42%	50%	55%	24%	45%	52%	57%
two_intervals	28%	42%	50%	48%	21%	42%	50%	51%
Average	26%	40%	50%	53%	23%	44%	51%	55%

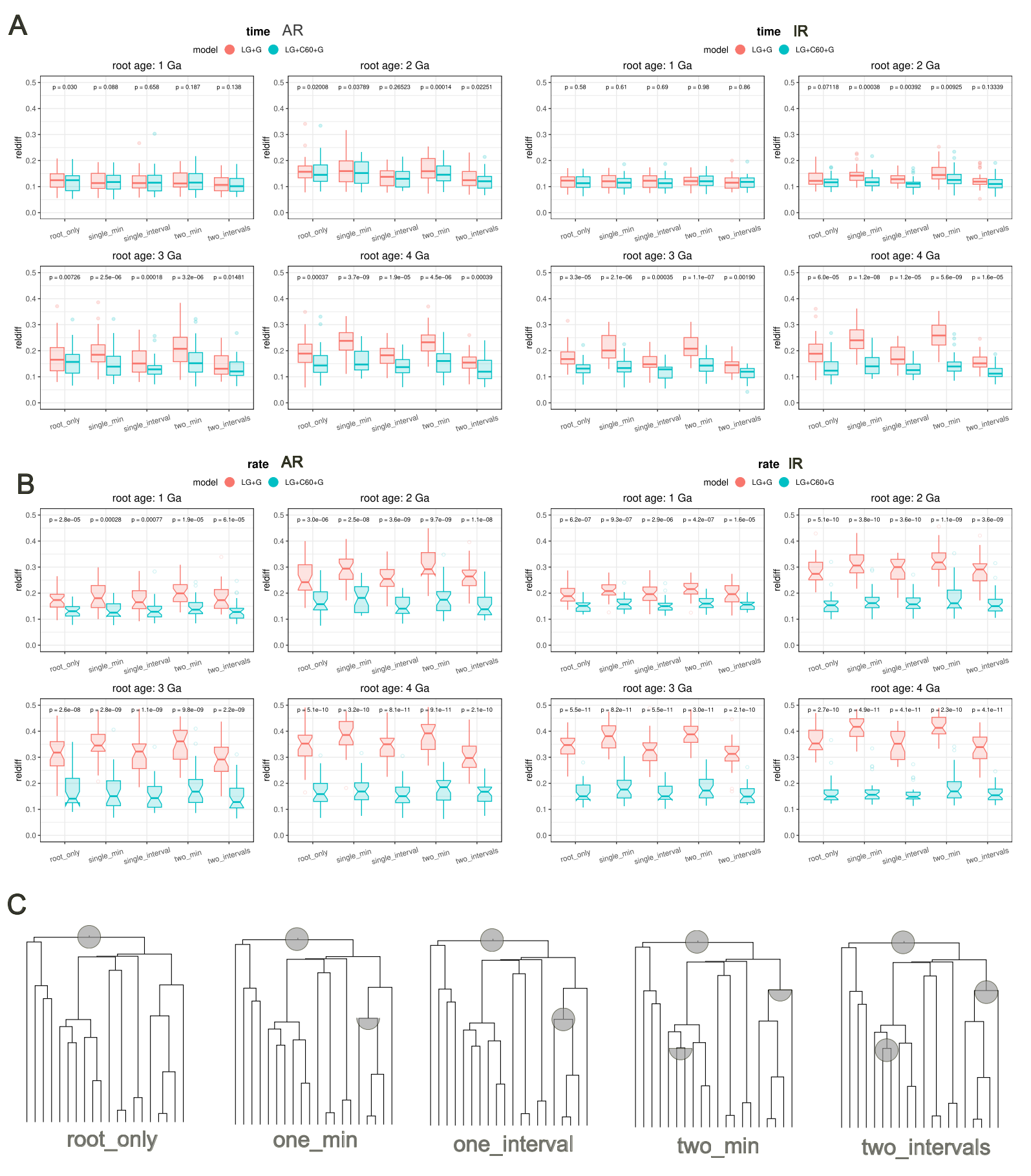
A
time AR
model LG+G LG+C60+G
root age: 1 Ga
p = 0.030 p = 0.088 p = 0.658 p = 0.187 p = 0.138
root age: 2 Ga
p = 0.02008 p = 0.03789 p = 0.26523 p = 0.00014 p = 0.02251
root age: 3 Ga
p = 0.00726 p = 2.5e−06 p = 0.00018 p = 3.2e−06 p = 0.01481
root age: 4 Ga
p = 0.00037 p = 3.7e−09 p = 1.9e−05 p = 4.5e−06 p = 0.00039
time IR
model LG+G LG+C60+G
root age: 1 Ga
p = 0.58 p = 0.61 p = 0.69 p = 0.98 p = 0.86
root age: 2 Ga
p = 0.07118 p = 0.00038 p = 0.00392 p = 0.00925 p = 0.13339
root age: 3 Ga
p = 3.3e−05 p = 2.1e−06 p = 0.00035 p = 1.1e−07 p = 0.00190
root age: 4 Ga
p = 6.0e−05 p = 1.2e−08 p = 1.2e−05 p = 5.6e−09 p = 1.6e−05
reldiff
root_only single_min single_interval two_min two_intervals
B
rate AR
model LG+G LG+C60+G
root age: 1 Ga
p = 2.8e−05 p = 0.00028 p = 0.00077 p = 1.9e−05 p = 6.1e−05
root age: 2 Ga
p = 3.0e−06 p = 2.5e−08 p = 3.6e−09 p = 9.7e−09 p = 1.1e−08
root age: 3 Ga
p = 2.6e−08 p = 2.8e−09 p = 1.1e−09 p = 9.8e−09 p = 2.2e−09
root age: 4 Ga
p = 5.1e−10 p = 3.2e−10 p = 8.1e−11 p = 9.1e−11 p = 2.1e−10
rate IR
model LG+G LG+C60+G
root age: 1 Ga
p = 6.2e−07 p = 9.3e−07 p = 2.9e−06 p = 4.2e−07 p = 1.6e−05
root age: 2 Ga
p = 5.1e−10 p = 3.8e−10 p = 3.6e−10 p = 1.1e−09 p = 3.6e−09
root age: 3 Ga
p = 5.5e−11 p = 8.2e−11 p = 5.5e−11 p = 3.0e−11 p = 2.1e−10
root age: 4 Ga
p = 2.7e−10 p = 4.9e−11 p = 4.1e−11 p = 2.3e−10 p = 4.1e−11
reldiff
root_only single_min single_interval two_min two_intervals
C
root_only
one_min
one_interval
two_min
two_intervals

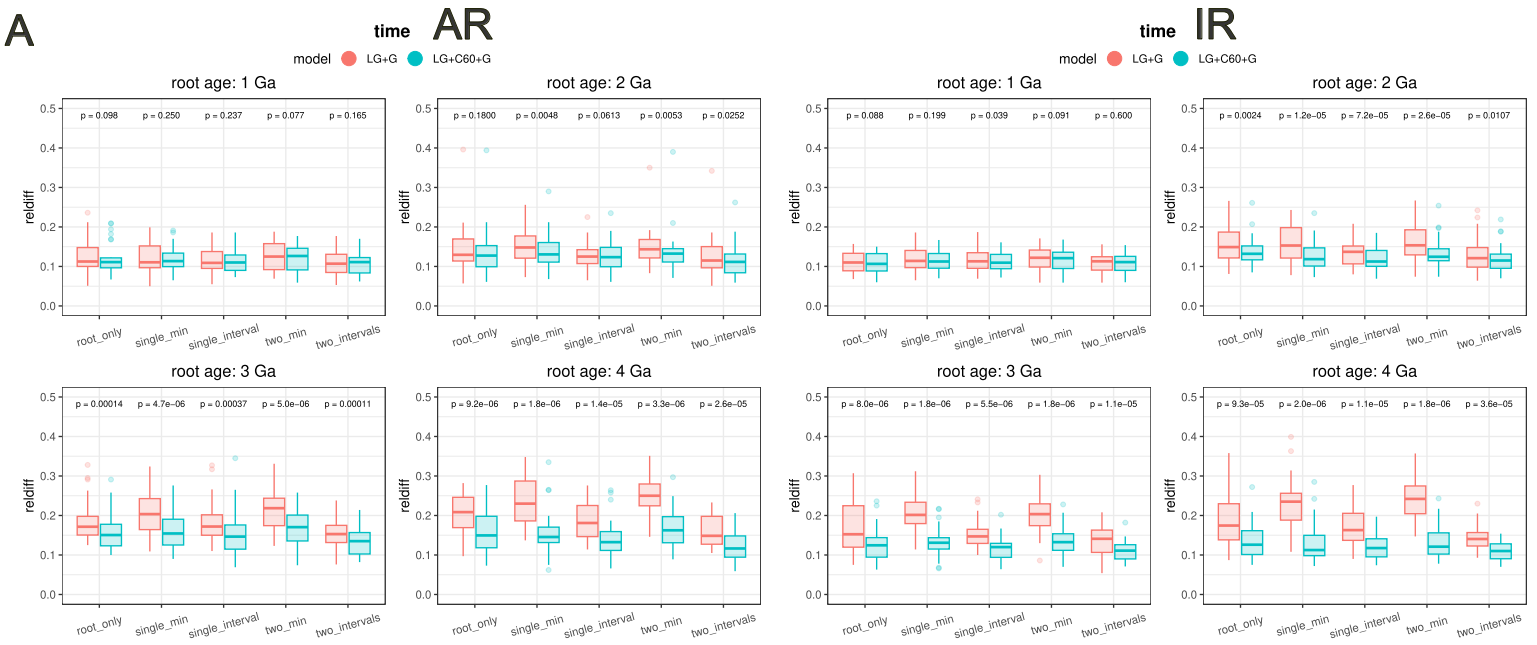
A
time
AR
model LG+G LG+C60+G
root age: 1 Ga
p = 0.098 p = 0.250 p = 0.237 p = 0.077 p = 0.165
root age: 2 Ga
p = 0.1800 p = 0.0048 p = 0.0613 p = 0.0053 p = 0.0252
root age: 3 Ga
p = 0.00014 p = 4.7e−06 p = 0.00037 p = 5.0e−06 p = 0.00011
root age: 4 Ga
p = 9.2e−06 p = 1.8e−06 p = 1.4e−05 p = 3.3e−06 p = 2.6e−05
time
IR
model LG+G LG+C60+G
root age: 1 Ga
p = 0.088 p = 0.199 p = 0.039 p = 0.091 p = 0.600
root age: 2 Ga
p = 0.0024 p = 1.2e−05 p = 7.2e−05 p = 2.6e−05 p = 0.0107
root age: 3 Ga
p = 8.0e−06 p = 1.8e−06 p = 5.5e−06 p = 1.8e−06 p = 1.1e−05
root age: 4 Ga
p = 9.3e−05 p = 2.0e−06 p = 1.1e−05 p = 1.8e−06 p = 3.6e−05
reldiff
0.0 0.1 0.2 0.3 0.4 0.5
root_only single_min single_interval two_min two_intervals

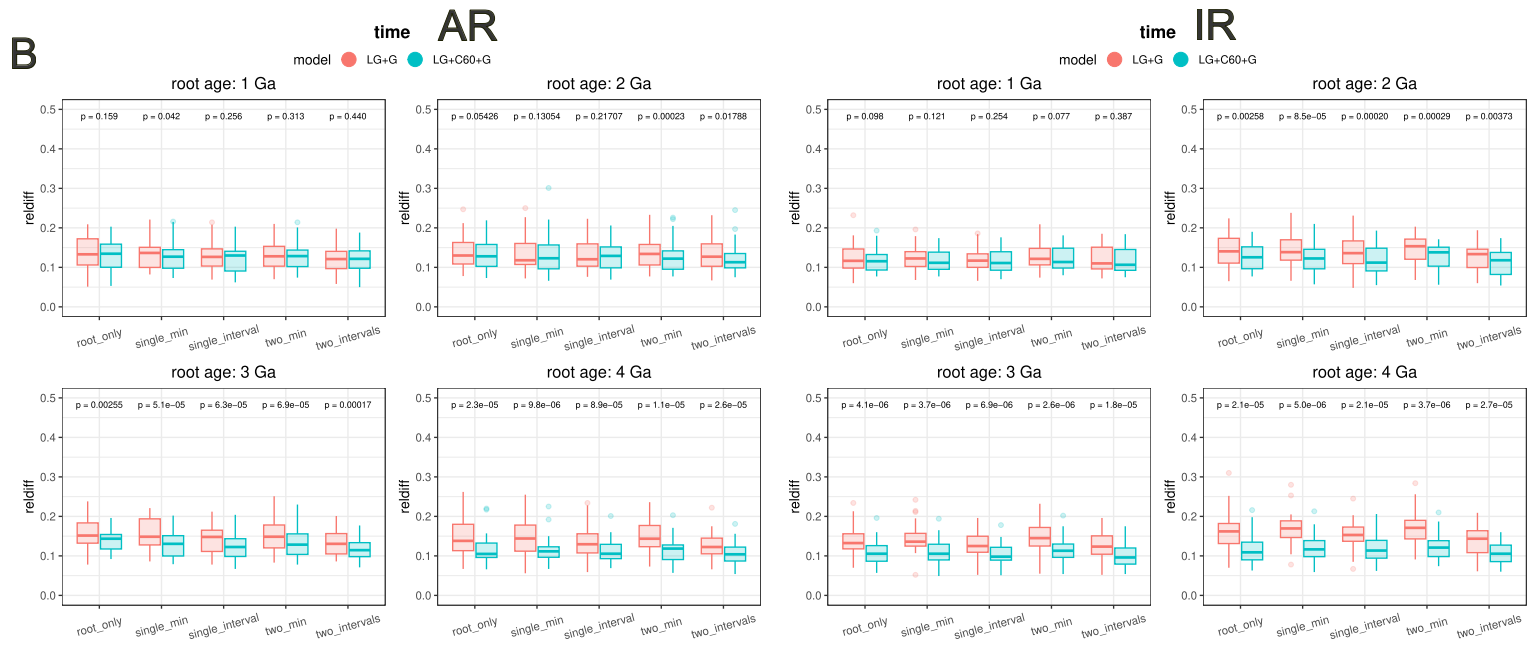
B
time
AR
model LG+G LG+C60+G
root age: 1 Ga
p = 0.159 p = 0.042 p = 0.256 p = 0.313 p = 0.440
root age: 2 Ga
p = 0.05426 p = 0.13054 p = 0.21707 p = 0.00023 p = 0.01788
root age: 3 Ga
p = 0.00255 p = 5.1e−05 p = 6.3e−05 p = 6.9e−05 p = 0.00017
root age: 4 Ga
p = 2.3e−05 p = 9.8e−06 p = 8.9e−05 p = 1.1e−05 p = 2.6e−05
time
IR
model LG+G LG+C60+G
root age: 1 Ga
p = 0.098 p = 0.121 p = 0.254 p = 0.077 p = 0.387
root age: 2 Ga
p = 0.00258 p = 8.5e−05 p = 0.00020 p = 0.00029 p = 0.00373
root age: 3 Ga
p = 4.1e−06 p = 3.7e−06 p = 6.9e−06 p = 2.6e−06 p = 1.8e−05
root age: 4 Ga
p = 2.1e−05 p = 5.0e−06 p = 2.1e−05 p = 3.7e−06 p = 2.7e−05
reldiff
0.0 0.1 0.2 0.3 0.4 0.5
root_only single_min single_interval two_min two_intervals

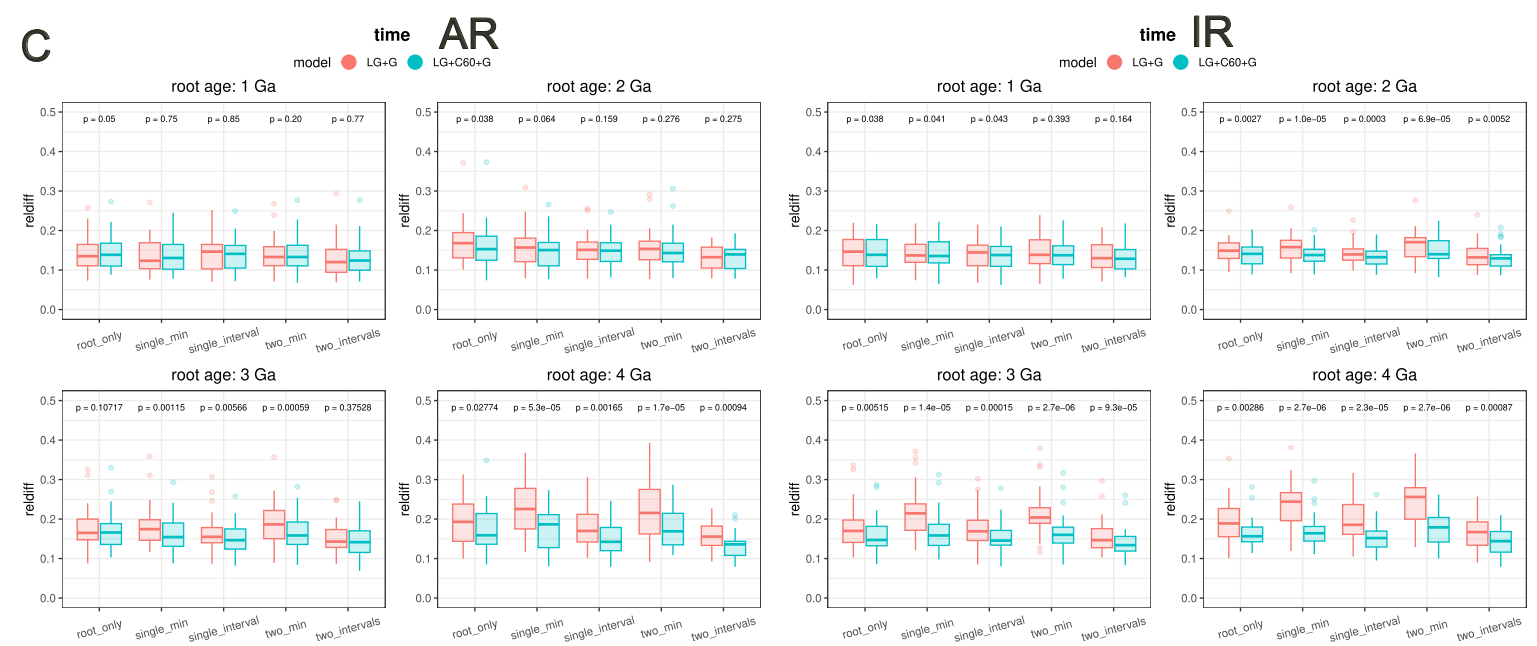
C
time
AR
model LG+G LG+C60+G
root age: 1 Ga
p = 0.05 p = 0.75 p = 0.85 p = 0.20 p = 0.77
root age: 2 Ga
p = 0.038 p = 0.064 p = 0.159 p = 0.276 p = 0.275
root age: 3 Ga
p = 0.10717 p = 0.00115 p = 0.00566 p = 0.00059 p = 0.37528
root age: 4 Ga
p = 0.02774 p = 5.3e−05 p = 0.00165 p = 1.7e−05 p = 0.00094
time
IR
model LG+G LG+C60+G
root age: 1 Ga
p = 0.038 p = 0.041 p = 0.043 p = 0.393 p = 0.164
root age: 2 Ga
p = 0.0027 p = 1.0e−05 p = 0.0003 p = 6.9e−05 p = 0.0052
root age: 3 Ga
p = 0.00515 p = 1.4e−05 p = 0.00015 p = 2.7e−06 p = 9.3e−05
root age: 4 Ga
p = 0.00286 p = 2.7e−06 p = 2.3e−05 p = 2.7e−06 p = 0.00087
reldiff
0.0 0.1 0.2 0.3 0.4 0.5
root_only single_min single_interval two_min two_intervals

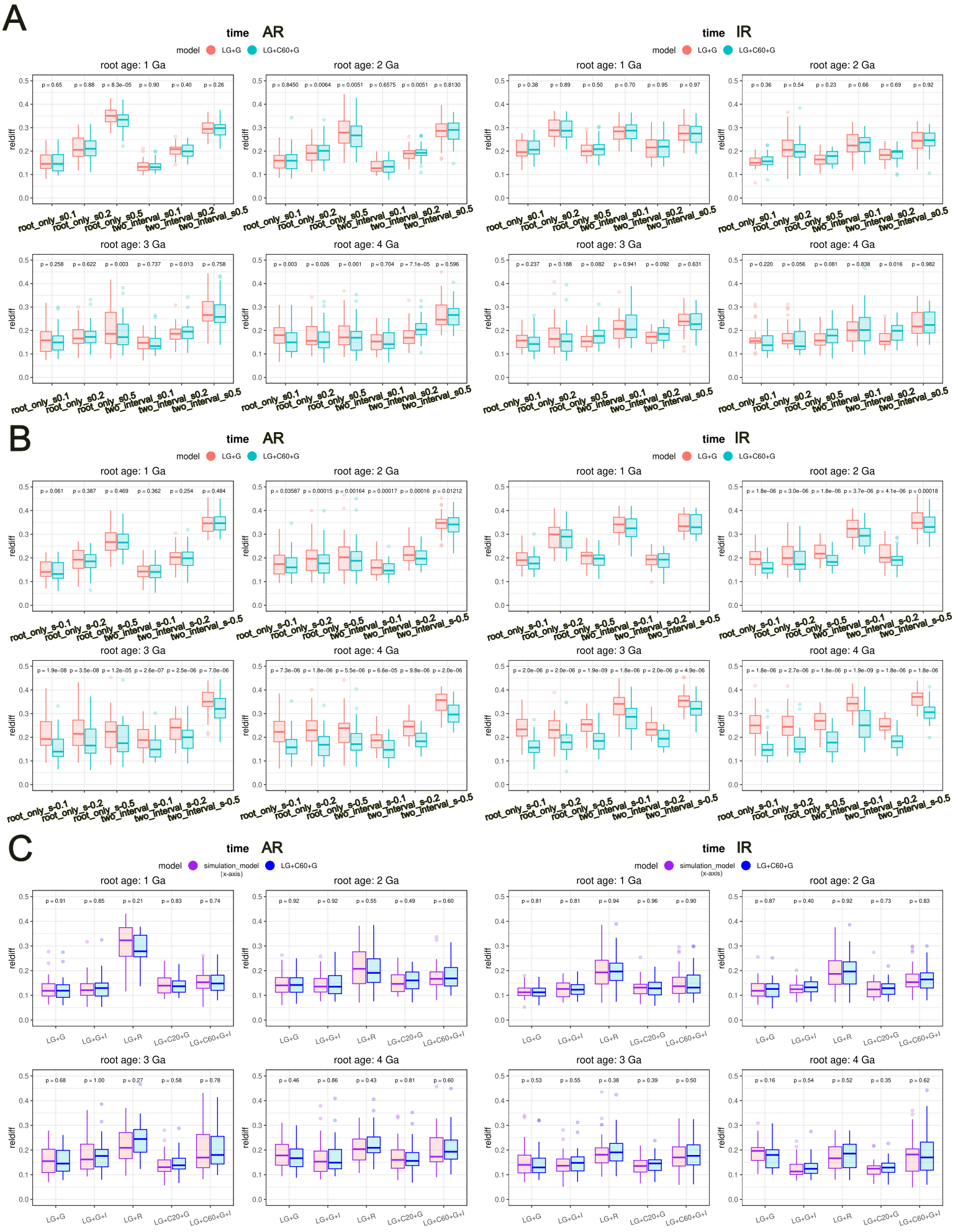
A
time AR
model LG+G LG+C60+G
root age: 1 Ga
p = 0.65 p = 0.88 p = 8.3e−05 p = 0.90 p = 0.40 p = 0.26
root age: 2 Ga
p = 0.8450 p = 0.0064 p = 0.0051 p = 0.6575 p = 0.0051 p = 0.8130
root age: 3 Ga
p = 0.258 p = 0.622 p = 0.003 p = 0.737 p = 0.013 p = 0.758
root age: 4 Ga
p = 0.003 p = 0.026 p = 0.001 p = 0.704 p = 7.1e−05 p = 0.596
time IR
model LG+G LG+C60+G
root age: 1 Ga
p = 0.38 p = 0.89 p = 0.50 p = 0.70 p = 0.95 p = 0.97
root age: 2 Ga
p = 0.36 p = 0.54 p = 0.23 p = 0.66 p = 0.69 p = 0.92
root age: 3 Ga
p = 0.237 p = 0.188 p = 0.082 p = 0.941 p = 0.092 p = 0.631
root age: 4 Ga
p = 0.220 p = 0.056 p = 0.081 p = 0.838 p = 0.016 p = 0.982
reldiff
root_only_s0.1 root_only_s0.2 root_only_s0.5 two_interval_s0.1 two_interval_s0.2 two_interval_s0.5
B
time AR
model LG+G LG+C60+G
root age: 1 Ga
p = 0.061 p = 0.387 p = 0.469 p = 0.362 p = 0.254 p = 0.484
root age: 2 Ga
p = 0.03587 p = 0.00015 p = 0.00164 p = 0.00017 p = 0.00016 p = 0.01212
root age: 3 Ga
p = 1.9e−08 p = 3.5e−08 p = 1.2e−05 p = 2.6e−07 p = 2.5e−06 p = 7.0e−06
root age: 4 Ga
p = 7.3e−06 p = 1.8e−06 p = 5.5e−06 p = 6.6e−05 p = 9.8e−06 p = 2.0e−06
time IR
model LG+G LG+C60+G
root age: 1 Ga
p = 1.8e−06 p = 3.0e−06 p = 1.8e−06 p = 3.7e−06 p = 4.1e−06 p = 0.00018
root age: 2 Ga
p = 2.0e−06 p = 2.0e−06 p = 1.9e−09 p = 1.8e−06 p = 2.0e−06 p = 4.9e−06
root age: 3 Ga
p = 1.8e−06 p = 2.7e−06 p = 1.8e−06 p = 1.9e−09 p = 1.8e−06 p = 1.8e−06
root age: 4 Ga
reldiff
root_only_s-0.1 root_only_s-0.2 root_only_s-0.5 two_interval_s-0.1 two_interval_s-0.2 two_interval_s-0.5
C
time AR
model simulation_model (x-axis) LG+C60+G
root age: 1 Ga
p = 0.91 p = 0.85 p = 0.21 p = 0.83 p = 0.74
root age: 2 Ga
p = 0.92 p = 0.92 p = 0.55 p = 0.49 p = 0.60
root age: 3 Ga
p = 0.68 p = 1.00 p = 0.27 p = 0.58 p = 0.78
root age: 4 Ga
p = 0.46 p = 0.86 p = 0.43 p = 0.81 p = 0.60
time IR
model simulation_model (x-axis) LG+C60+G
root age: 1 Ga
p = 0.81 p = 0.81 p = 0.94 p = 0.96 p = 0.90
root age: 2 Ga
p = 0.87 p = 0.40 p = 0.92 p = 0.73 p = 0.83
root age: 3 Ga
p = 0.53 p = 0.55 p = 0.38 p = 0.39 p = 0.50
root age: 4 Ga
p = 0.16 p = 0.54 p = 0.52 p = 0.35 p = 0.62
reldiff
LG+G LG+G+I LG+R LG+C20+G LG+C60+G+I

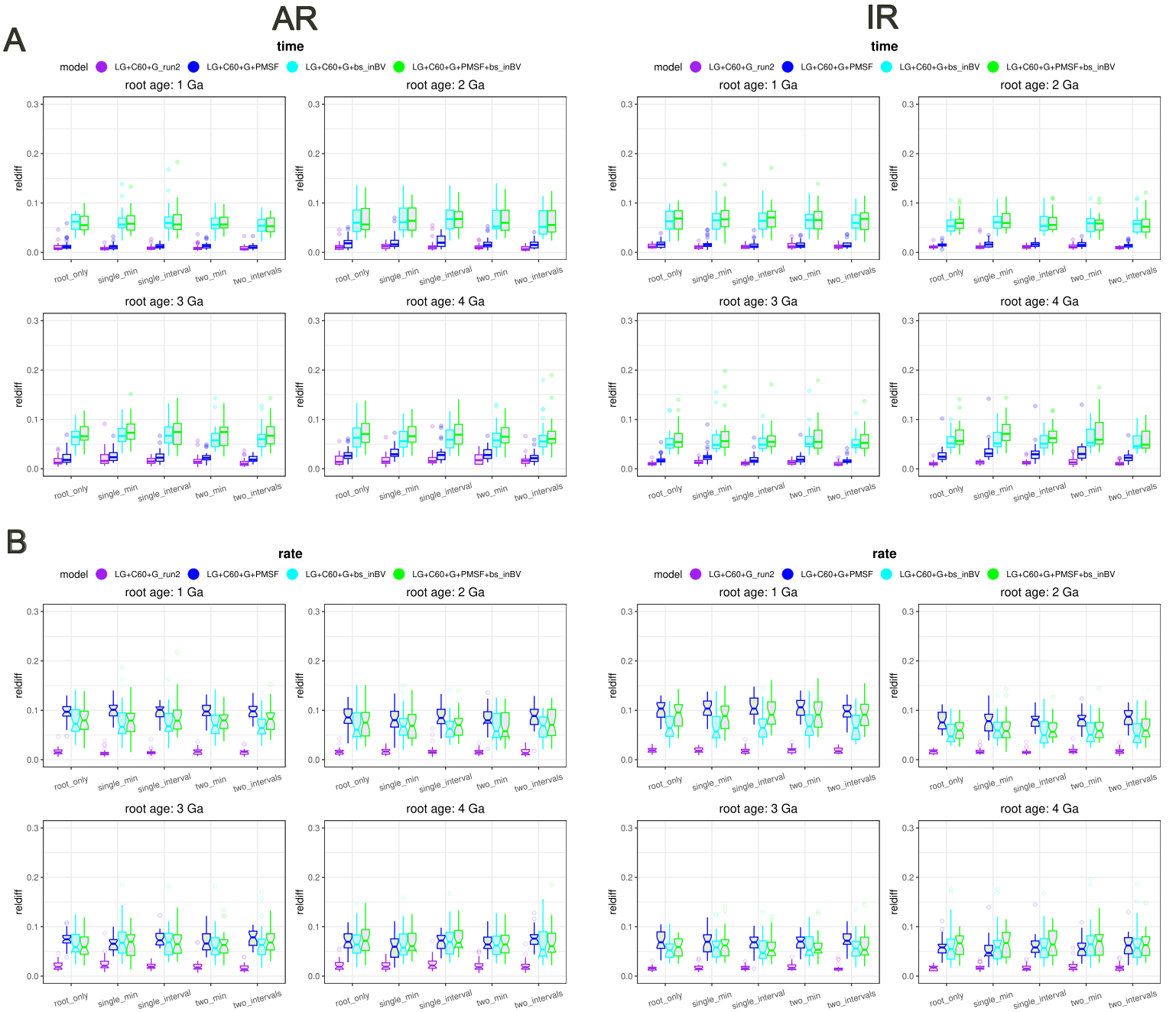
A
AR
IR
time
rate
model
LG+C60+G_run2
LG+C60+G+PMSF
LG+C60+G+bs_inBV
LG+C60+G+PMSF+bs_inBV
root age: 1 Ga
root age: 2 Ga
root age: 3 Ga
root age: 4 Ga
reldiff
0.0
0.1
0.2
0.3
root_only
single_min
single_interval
two_min
two_intervals
B

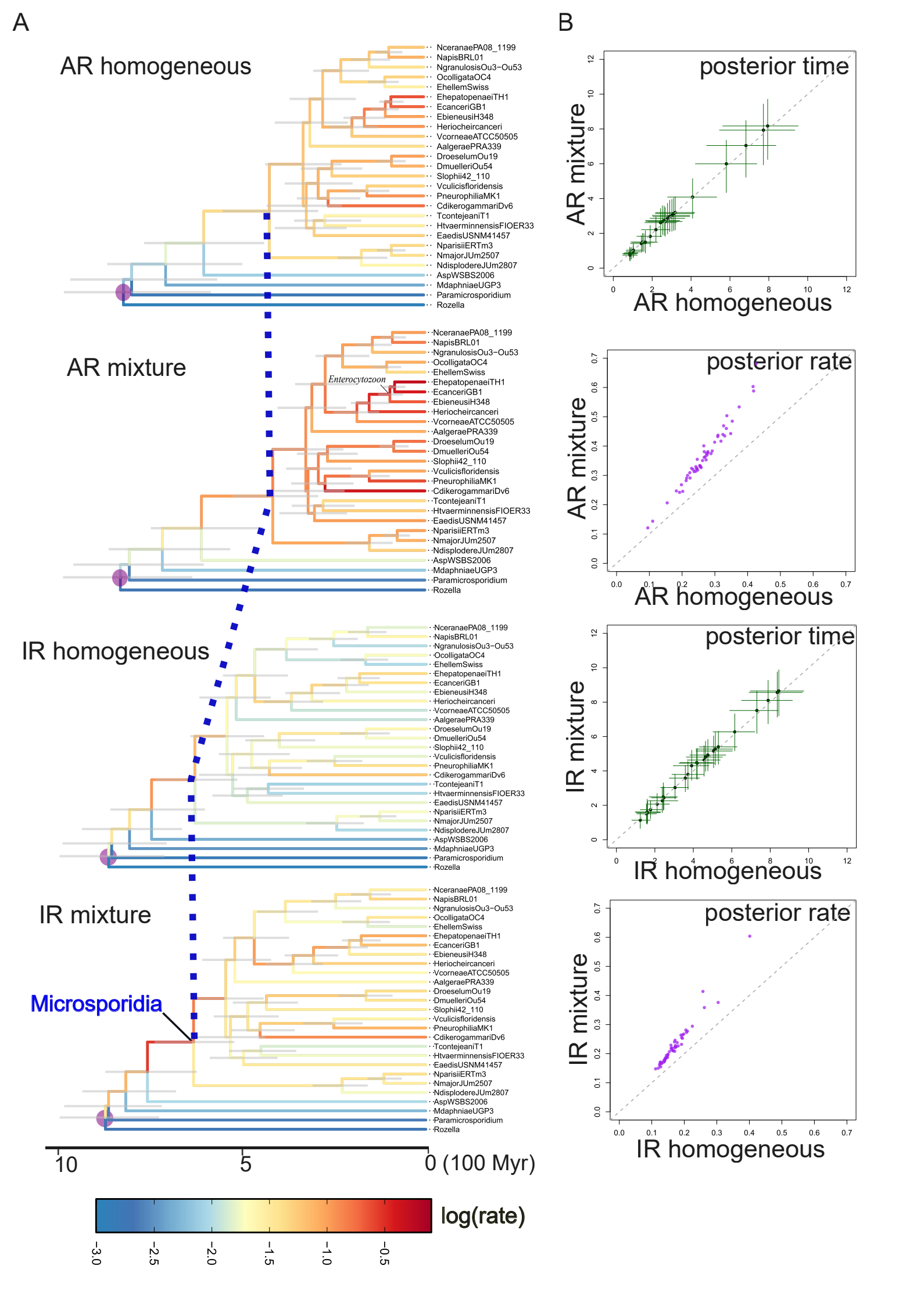
A
AR homogeneous
AR mixture
IR homogeneous
IR mixture
Microsporidia
Enterocytozoon
NceranaePA08_1199
NapisBRL01
NgranulosisOu3−Ou53
OcolligataOC4
EhellemSwiss
EhepatopenaeiTH1
EcanceriGB1
EbieneusiH348
Heriocheircanceri
VcorneaeATCC50505
AalgeraePRA339
DroeselumOu19
DmuelleriOu54
Slophii42_110
Vculicisfloridensis
PneurophiliaMK1
CdikerogammariDv6
TcontejeaniT1
HtvaerminnensisFIOER33
EaedisUSNM41457
NparisiiERTm3
NmajorJUm2507
NdisplodereJUm2807
AspWSBS2006
MdaphniaeUGP3
Paramicrosporidium
Rozella
10
5
0 (100 Myr)
log(rate)
−3.0
−2.5
−2.0
−1.5
−1.0
−0.5
B
posterior time
AR mixture
AR homogeneous
posterior rate
AR mixture
AR homogeneous
posterior time
IR mixture
IR homogeneous
posterior rate
IR mixture
IR homogeneous

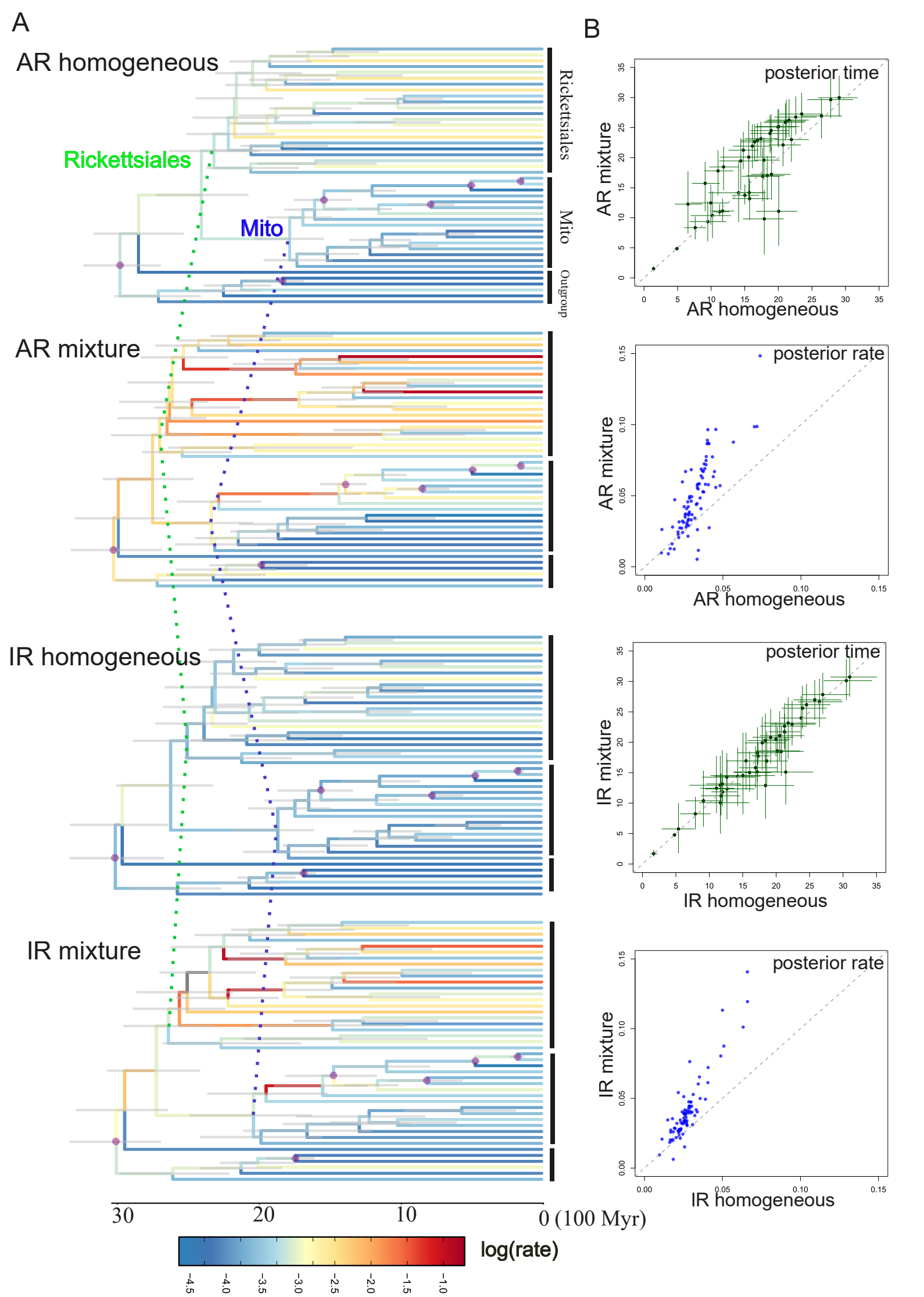
A
AR homogeneous
Rickettsiales
Mito
Rickettsiales
Mito
Outgroup
AR mixture
IR homogeneous
IR mixture
30
20
10
0 (100 Myr)
log(rate)
-4.5
-4.0
-3.5
-3.0
-2.5
-2.0
-1.5
-1.0
B
posterior time
AR mixture
AR homogeneous
posterior rate
AR mixture
AR homogeneous
posterior time
IR mixture
IR homogeneous
posterior rate
IR mixture
IR homogeneous